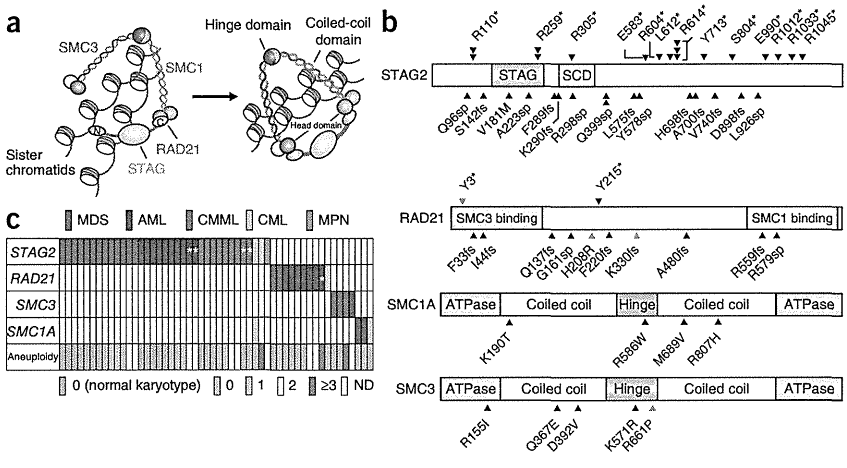

Figure 1 Genetic alterations of the cohesin complex in myeloid neoplasms. (**a**) Cohesin holds chromatin strands within a ring-like structure that is composed of four core components STAG, RAD21, SMC1 and SMC3. (**b**) Mutations in the core components of the cohesin complex found in myeloid malignancies (black arrowheads) and myeloid leukemia-derived cell lines (blue arrowheads). The amino acids in the alterations are referred to using their one-letter abbreviations (for example, R110* represents p.Arg110*). (**c**) Distribution of cohesin mutations and deletions showing a nearly mutually exclusive pattern among different myeloid neoplasms. Gene deletions are indicated by asterisks. The number of numerical chromosome abnormalities in each cohesin-mutated or -deleted case is shown at the bottom. ND, not determined.

and STAG proteins, together with a number of regulatory molecules such as PDS5, NIPBL and ESCO proteins (**Fig. 1a**)[4,5]. Forming a ring-like structure, cohesin is thought to be engaged in the cohesion of sister chromatids during cell division[5], post-replicative DNA repair[6,7] and the regulation of global gene expression through long-range *cis* interactions[8–12]. Germline mutations in cohesin components lead to the congenital multisystem malformation syndromes known as Cornelia de Lange syndrome and Roberts syndrome[13–15].

To investigate a possible role of cohesin mutations in myeloid leukemogenesis, we examined an additional 581 primary specimens of various myeloid neoplasms for mutations in nine cohesin or cohesin-related genes that have been implicated in mitosis[5] using high-throughput sequencing (**Supplementary Table 2**). We also investigated copy-number alterations in cohesin loci in 453 samples using SNP arrays (**Supplementary Table 3**). After excluding known and putative polymorphisms that are registered in the dbSNP or the *1000 Genomes* project databases or that were predicted from multiple computational imputations, we identified a total of 60 nonsynonymous mutations involving nine genes in a total of 610 primary samples, which we validated by Sanger sequencing (**Fig. 1b** and **Supplementary Table 4**). After conservative evaluation of the probability of random mutational events across these genes, only four genes remained significantly mutated: *STAG2*, *RAD21*, *SMC1A* and *SMC3* ($P < 0.001$) (**Supplementary Table 5** and Online Methods). In addition, we detected five deletions in *STAG2* ($n = 4$) and *RAD21* ($n = 1$) (**Supplementary Fig. 2a,b** and **Supplementary Table 6**). We also found mutations in these four genes in four of the 34 myeloid leukemia cell lines studied (12%) (**Supplementary Table 7**).

We found mutations and deletions of these four genes in a mostly mutually exclusive manner in a variety of myeloid neoplasms, including acute myeloid leukemia (AML) (19/157), chronic myelomonocytic leukemia (CMML) (9/88), myelodysplastic syndromes (MDS) (18/224) and chronic myelogenous leukemia (CML) (4/64). Mutations were rate in classical myeloproliferative neoplasms (MPN) (1/77) (**Fig. 1c**, **Table 1** and **Supplementary Table 8**). In MDS, mutations were more frequent in refractory cytopenia with multilineage dysplasia and refractory anemia with excess blasts (11.4%) but were rare in refractory anemia, refractory anemia with ring sideroblasts, refractory cytopenia with multilineage dysplasia and ring sideroblasts and MDS with isolated del(5q) (4.2%) ($P = 0.044$). We also evaluated promoter methylation in 33 cases either with ($n = 12$) or without ($n = 21$) cohesin mutations or deletions for which sufficient nonamplified DNA was available using the HumanMethylation450 BeadChip; however, we found no aberrant methylations in cohesin loci, with the exception of hemimethylation of the *SMC1A* promoter that we found in two female cases (**Supplementary Fig. 3**).

We confirmed somatic origins for 17 mutations detected in 16 cases for which matched normal DNA was available (**Supplementary Table 4**). The somatic origins of an additional 23 mutations in *STAG2* or *SMC1A* found in 20 male cases were supported by the presence of reproducible wild-type signals or reads in Sanger and/or deep sequencing of the tumor samples, which were considered to originate from the X chromosome of the residual normal cells (**Supplementary Fig. 4**). In addition, for 20 mutations, the observed allele frequencies determined by pyrosequencing, deep sequencing or digital PCR showed significant deviations from the expected value for polymorphisms in the absence of apparent chromosomal alterations in a SNP array analysis ($P < 0.01$) (**Supplementary Figs. 5** and **6** and **Supplementary Tables 9–12**), suggesting their somatic origins. In addition, 32 of the 33 *STAG2* mutations and all of the nine *RAD21* mutations were either nonsense ($n = 18$), frameshift ($n = 14$) or splice-site ($n = 9$) changes, which were predicted to cause premature truncation of the protein or abnormal exon skipping (**Fig. 1b** and **Supplementary Figs. 7** and **8**). Thus, we considered the majority of the mutations to represent functionally relevant changes, probably of somatic origins (**Supplementary Table 13**).

Most of the cohesin mutations and deletions were heterozygous, except for the *STAG2* and *SMC1A* mutations on the single X chromosome in male cases ($n = 23$). In female samples, the *STAG2* promoter

Table 1 Frequencies of mutations and deletions of cohesin components in 610 myeloid neoplasms

Disease type	*n*	*STAG2*	*RAD21*	*SMC1A*	*SMC3*	Total	Percentage
MDS	224	13	2	0	3	18	8.0
CMML	88	9[a]	0	0	0	9	10.2
AML	157	10	7	2	1	19	12.1
de novo AML	120	8[a]	6	2	1	16	13.3
AML/MRC	37	2[a]	1[a]	0	0	3	8.1
CML	64	2[b]	1	2[b]	0	4	6.3
MPN	77	1	0	0	0	1	1.3
Total	610	35[b]	10	4[b]	4	52	8.5

Diseases are classified according to the World Health Organization 2008 classification. AML/MRC, AML with myelodysplasia-related changes.
[a] Two of the nine cases with *STAG2* alterations in CMML, one of the eight cases with *STAG2* alterations in *de novo* AML, one of the two cases with *STAG2* alterations in AML/MRC cases and one case with *RAD21* alteration in AML/MRC case involved genetic deletions. [b] One CML case having mutations in both *STAG2* and *SMC1A* was counted as a single case. A more detailed list is available in **Supplementary Table 8**.

Figure 2 Relationship between cohesin mutations and other common mutations in myeloid malignancies. (**a**) Mutations in the cohesin complex and other common targets in 310 cases with different myeloid neoplasms. The corresponding disease types are shown in the bottom lane. *IDH1/2*, either *IDH1* or *IDH2*. AML/MRC, AML with myelodysplasia-related changes. (**b**) Allele frequencies of mutations in cohesin components and other coexisting mutations in 20 myeloid neoplasms determined by deep sequencing.

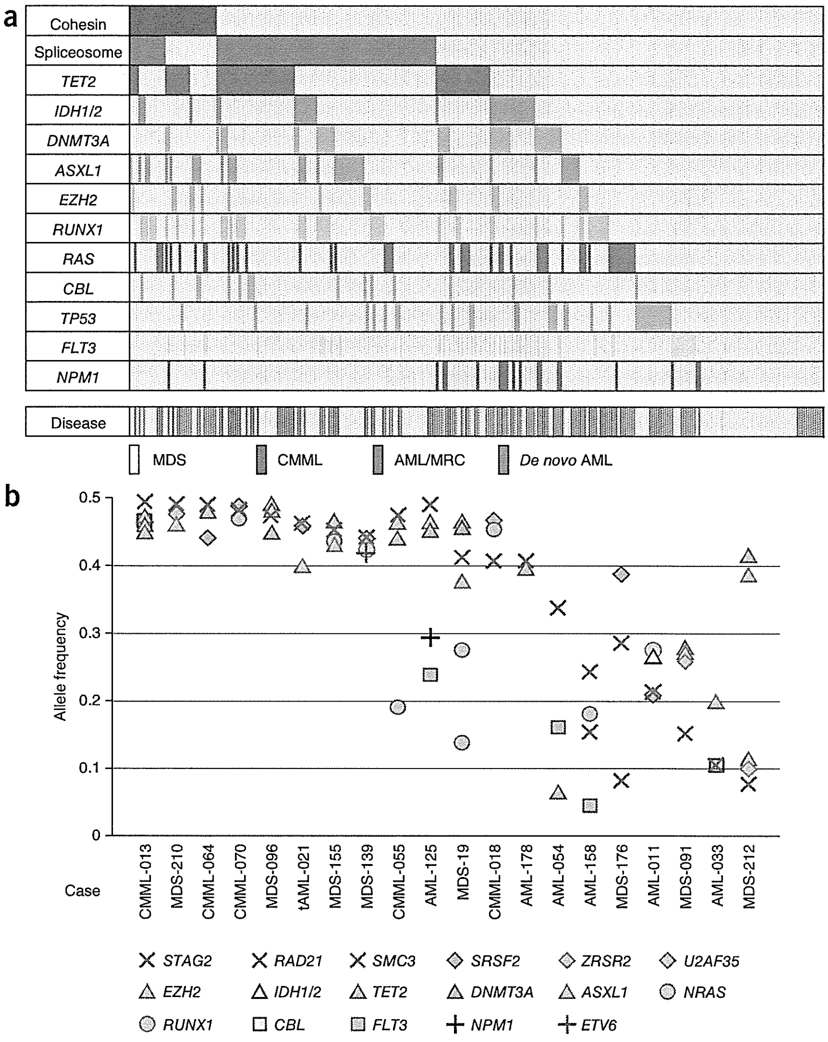

was hemimethylated through X inactivation regardless of mutation status (**Supplementary Fig. 3**), and a heterozygous mutation of the unmethylated *STAG2* allele would lead to biallelic *STAG2* inactivation, as has been previously documented in a female case with Ewing's sarcoma[16] and was also confirmed in a single case (CMML-036) in our cohort (**Supplementary Fig. 9**).

Cohesin mutations frequently coexisted with other mutations that are common in myeloid neoplasms and significantly associated with mutations in *TET2* ($P = 0.027$), *ASXL1* ($P = 0.045$) and *EZH2* ($P = 0.011$) (**Fig. 2a**). We performed deep sequencing of the mutant alleles in 20 available samples with cohesin mutations, which allowed for accurate determination of their allele frequencies. The majority of the cohesin mutations (15/20) existed in the major tumor populations, indicating their early origin during leukemogenesis. In the remaining five samples, we found cohesin mutations only in a tumor subpopulation, indicating that the mutations were relatively late events (**Fig. 2b**). Two male cases (MDS-176 and AML-158) harbored two independent subclones with different *STAG2* mutations, indicating that *STAG2* mutation could confer a strong advantage to pre-existing leukemic cells during clonal evolution (**Supplementary Fig. 10**). The number of mutations determined by whole-exome sequencing[3] was significantly higher in four cases with cohesin mutation or deletion compared to cases with no mutation or deletion of cohesin ($P = 0.049$) (**Supplementary Fig. 11**).

Next we investigated the possible impact of mutations on cohesin function. We examined the expression of STAG1, STAG2, RAD21, SMC3, SMC1A and NIPBL in 17 myeloid leukemia cell lines with ($n = 4$) or without ($n = 13$) known cohesin mutations, as well as in the chromatin-bound fractions of 13 cell lines (**Fig. 3a–d** and **Supplementary Table 14**)[14,17–19]. Although we observed an evaluable reduction in RAD21 expression in Kasumi-1 cells that harbored a frameshift alteration in RAD21 (p.Lys330ProfsX6) (**Fig. 3a**), alterations in P31FUJ (RAD21 p.His208Arg), CMY (RAD21 p.Tyr3X) and MOLM-7 (SMC3 p.Arg661Pro) cells were not accompanied by measurable decreases in the corresponding mutated proteins compared to wild-type cell lines. In contrast, we observed severely reduced expression of one or more cohesin components in KG-1 (STAG2)[16] and MOLM-13 (STAG1, STAG2, RAD21 and NIPBL) cells without any accompanying mutations in the relevant genes (**Fig. 3a**). We found no significant differences in protein expression of the cohesin components in cohesin-mutated and non-mutated cell lines in whole-cell extracts (**Fig. 3b**). However, expression of one or more cohesin components, including SMC1, SMC3, RAD21 and STAG2, was significantly reduced in the chromatin-bound fractions of cell lines with mutated or reduced expression of cohesin components, including Kasumi-1, KG-1, P31FUJ, MOLM-7 and MOLM-13 cells, compared with the cell lines with no known cohesin mutations or abnormal cohesin expression ($P < 0.05$), suggesting a substantial loss of cohesin-bound sites on chromatin (**Fig. 3c,d** and **Supplementary Table 14**)[14].

We next examined the effect of forced expression of wild-type cohesin components on the proliferation of a cohesin-mutated cell line (Kasumi-1) or a cell line with reduced expression of cohesin components (MOLM-13). Forced expression of wild-type *RAD21* and/or *STAG2*, but not of a truncated *RAD21* allele, induced significant growth suppression of the Kasumi-1 (with mutated *RAD21*) and MOLM-13 (with severe reduction of RAD21 and STAG2 expression) cell lines but not the K562 and TF1 (with wild-type *RAD21*) cell lines, supporting a leukemogenic role for compromised cohesin functions (**Fig. 4a–c** and **Supplementary Fig. 12a–g**). To explore the effect of forced expression of RAD21 on global gene expression, we performed expression microarray analysis of *RAD21*- and mock-transduced Kasumi-1 cells. In agreement with previous experiments with other cohesin and cohesin-related components, the magnitudes of the

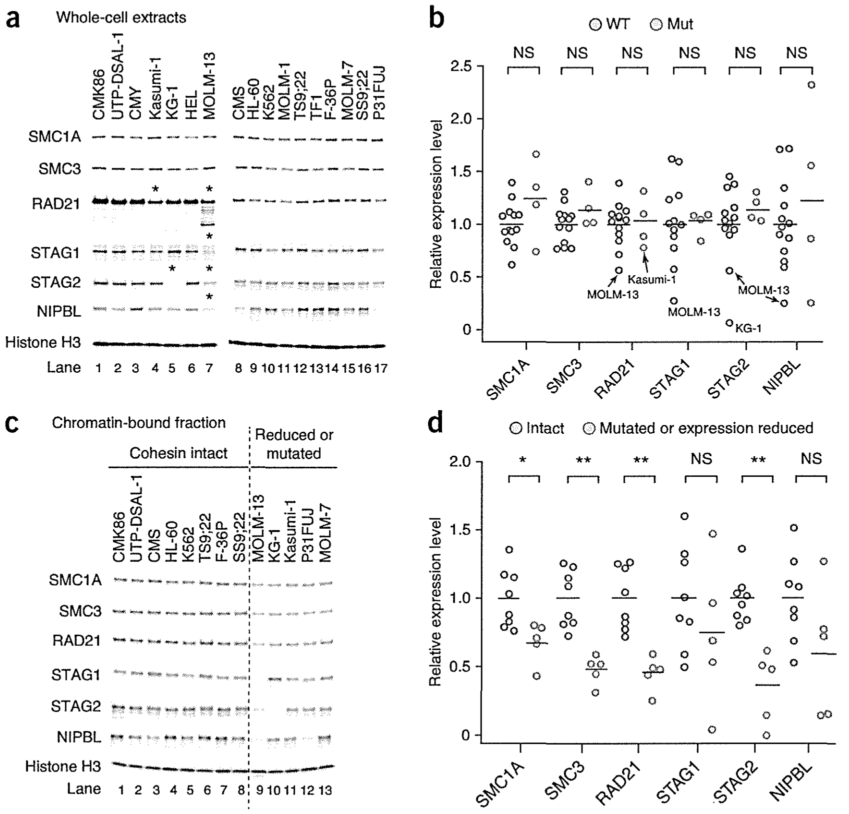

Figure 3 Abnormal cohesin expression and chromatin binding of various cohesin components in myeloid leukemic cell lines. (**a**) Protein blot analysis of the expression of various cohesin components in whole-cell extracts in 17 myeloid leukemia cell lines. Cohesin components showing evaluable reduction in expression are indicated by asterisks, which were reproducible in two independent experiments. (**b**) Expression levels of each cohesin component measured by densitometry after normalization for the mean value across all non-mutated cell lines, with histone H3 signals serving as controls. Evaluably reduced RAD21 expression in Kasumi-1 cells and severely reduced expression of cohesin components in MOLM-13 and KG-1 cells are indicated within the plots. No significant differences (NS) in the expression of the cohesin components were observed between cohesin-mutated and non-mutated cell lines (Mann-Whitney *U* test). Each circle represents a single cell line. (**c**) Protein blot analysis of cohesin components in the chromatin-bound fractions of 13 myeloid leukemia cell lines having intact cohesin (lanes 1–8), cohesin mutations and/or reduced expression of cohesin in whole-cell extracts (lanes 9–13). A representative result of two independent experiments reproducibly showing reduced chromatin-bound cohesin fractions in the cell lines in lanes 9–13 is presented. (**d**) Expression levels of cohesin components in the chromatin-bound fractions measured by densitometry after normalization for the mean value across cell lines with intact cohesin components, with histone H3 signals serving as controls. $^{*}P < 0.05$, $^{**}P < 0.005$ (Mann-Whitney *U* test). Horizontal bars in **b** and **d** indicate the mean values. The densitometric data are presented in **Supplementary Table 14**.

transcriptional changes induced by forced RAD21 expression were generally small[14,16,20]. However, 63 genes reproducibly and significantly showed a more than 1.2-fold increase ($n = 35$) or decrease ($n = 28$) in gene expression ($P < 0.05$), which was validated by quantitative PCR and/or RNA sequencing for 59 of the 63 genes (**Supplementary Fig. 13a–c** and **Supplementary Tables 15** and **16**).

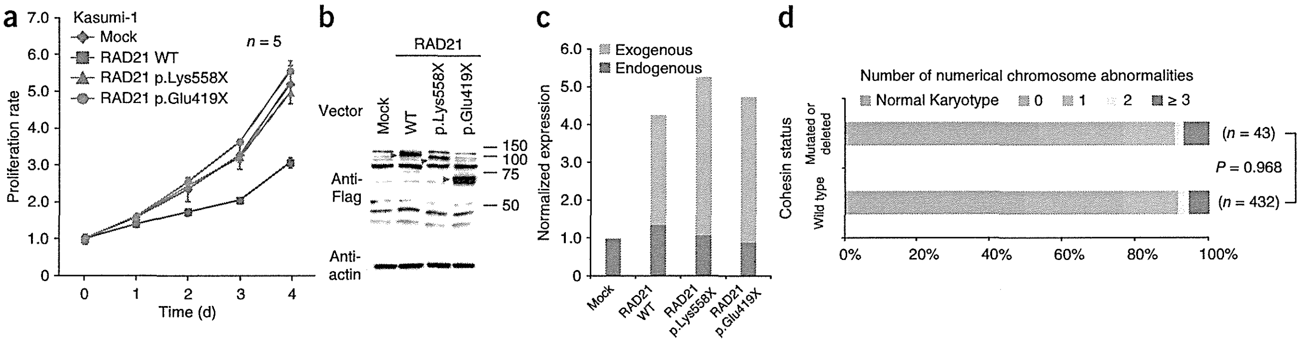

Figure 4 Impact of cohesin mutations on cell proliferation and karyotypes. (**a**) Proliferation of the Kasumi-1 cell line stably transduced with either wild-type RAD21, a truncated allele of *RAD21* (RAD21 p.Lys558X or p.Glu419X) or a mock construct measured by MTT assays ($n = 5$ wells per group). The data are shown as the means ± s.d. of the absorbance at 450 nm relative to the value at day 0. Representative results of three independent experiments are shown. (**b**) Protein blot analysis showing expression of the transduced wild-type and mutant RAD21 alleles. (**c**) Expression of endogenous and exogenous *RAD21* transcripts in Kasumi-1 cells transduced with indicated constructs measured using RNA sequencing by enumerating the corresponding reads. (**d**) The numbers of cases with numerical cytogenetic abnormalities were compared between two groups, those with and those without cohesin mutations or deletions ($P = 0.968$, χ^2). The numbers of numerical chromosome abnormalities are shown at the top. (**e**) Representative metaphases of cell lines with intact (CMS) or abnormal (Kasumi-1 and MOLM-13) cohesin components showing almost normal sister chromatid cohesion. Scale bars, 10 µm.

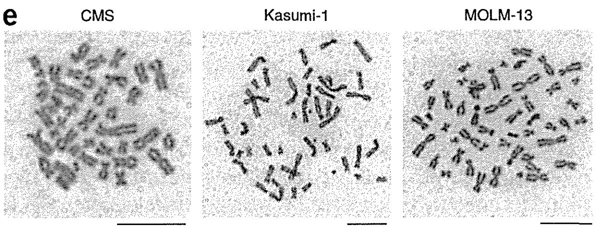

Mutations in the cohesin complex have recently been reported in a cohort of *de novo* AML and MDS in which four major cohesin components were mutated in 6.0–13.0% of cases[21–25]. Less frequent mutations of cohesin components have been described in other cancers, including *STAG2* mutations in glioblastoma (4/68), melanoma (1/48) and Ewing's sarcoma (1/24)[16]. In primary colon cancer samples, in which impaired cohesion and consequent aneuploidy have been implicated in oncogenesis, mutations in *SMC1A* (4/132), *NIPBL* (4/132), *STAG3* (1/130) and *SMC3* (1/130) have been reported[26]. In contrast, in our cohort of myeloid neoplasms, we found no significant differences in the number of numerical chromosome abnormalities between cohesin-mutated and non-mutated cases, and the 43 cases with cohesin mutations or deletions showed diploid or near-diploid karyotypes, including 23 cases with completely normal karyotypes (**Fig. 4d**). Therefore, in these euploid cases, cohesin-mutated cells were not clonally selected as a result of aneuploidy. Supporting this finding is the observation that expression of *scc1p*, a *RAD21* homolog, at only 13% of its normal level was sufficient for normal cohesion in yeast[27]. Furthermore, Kasumi-1 and MOLM-13 cells showed almost normal cohesion of sister chromatids, even though Kasumi-1 cells have a truncated *RAD21* allele and MOLM-13 cells have substantially reduced expression of multiple cohesin components (**Fig. 4e**).

A growing body of evidence has suggested that cohesin mediates long-range chromosomal *cis* interactions[28] and regulates global gene expression[11,12]. For example, two cohesin subunits, Rad21 and Smc3, have been implicated in the transcriptional regulation of the hematopoietic transcription factor Runx1 in zebrafish[10]. Furthermore, an up to 80% downregulation of *Nipped-B*, a *NIPBL* homolog in *Drosophila*, does not affect chromosomal segregation but does cause impaired regulation of gene expression[20]. We also previously demonstrated that only mild loss (17–28%) of cohesin binding sites within the genome results in deregulated global gene expression[14,18,19]. These observations suggest the possibility that cohesin mutations participate in leukemogenesis through the deregulated expression of genes that are involved in myeloid development and differentiation.

In conclusion, we report frequent mutations in cohesin components that involve a wide variety of myeloid neoplasms. Genetic evidence suggests that aneuploidy may not be the only leukemogenic mechanism, at least *in vivo*, and that deregulated gene expression and/or other mechanisms, such as DNA hypermutability, might also operate in leukemogenesis. Given the integral functions of cohesin for cell viability, genetic defects in cohesin might be potential targets in myeloid neoplasms[14,29].

URLs. dbSNP, http://www.ncbi.nlm.nih.gov/projects/SNP/; the 1000 Genomes Project, http://www.1000genomes.org/; the UCSC Genome Browser; http://genome.ucsc.edu/cgi-bin/hgGateway/; hg19, http://hgdownload.cse.ucsc.edu/goldenPath/hg19/database/; RefSeq genes, http://www.ncbi.nlm.nih.gov/RefSeq/; CNAG/AsCNAR, http://www.genome.umin.jp/; dChip, http://www.dchip.org/; the Integrative Genomics Viewer, http://www.broadinstitute.org/igv/; SIFT, http://sift.jcvi.org/; PolyPhen-2, http://genetics.bwh.harvard.edu/pph2/; Mutation Taster, http://www.mutationtaster.org/.

METHODS

Methods and any associated references are available in the online version of the paper.

Accession codes. Whole-exome sequence data have been deposited in the DNA Data Bank of Japan (DDBJ) repository under accession number DRA000433. RNA sequencing data have been deposited in the DDBJ repository under accession number DRA001013. Microarray data have been deposited in the Gene Expression Omnibus under accession number GSE47684.

Note: Any Supplementary Information and Source Data files are available in the online version of the paper.

ACKNOWLEDGMENTS

This work was supported by Grants-in-Aid from the Ministry of Health, Labor and Welfare of Japan and KAKENHI (23249052, 22134006 and 21790907; S.O.), the Industrial Technology Research Grant Program from the New Energy and Industrial Technology Development Organization (NEDO; S.O.) (08C46598a), NHRI-EX100-10003NI Taiwan (L.-Y.S.), the project for development of innovative research on cancer therapies (p-direct; S.O.) and the Japan Society for the Promotion of Science through the Funding Program for World-Leading Innovative R&D on Science and Technology, initiated by the Council for Science and Technology Policy (CSTP; S.O.). We thank Y. Hayashi (Gunma Children's Medical Centre), R.C. Mulligan (Harvard Medical School), S. Sugano (The University of Tokyo), M. Onodera (National Center for Child Health and Development, Japan) and L. Ström (Karolinska Institute) for providing materials. We thank Y. Yamazaki for cell sorting. We also thank Y. Mori, M. Nakamura, N. Mizota and S. Ichimura for their technical assistance and M. Ueda for encouragement.

AUTHOR CONTRIBUTIONS

A.K., Y.N., K.Y., A.S.-O., Y. Sato and M.S. processed and analyzed genetic materials and performed sequencing and SNP array analysis. Y. Shiraishi, Y.O., R.N., A.S.-O., H.T., T.S., K.C., M.N. and S. Miyano performed bioinformatics analyses of the sequencing data. L.-Y.S. performed pyrosequencing analysis, and A.N. and S.I. performed digital PCR. G.N. and H.A. performed methylation analysis. M.M., M.B. and K.S. performed studies on protein expression of cohesin components. A.K., M.S., T.Y., R.Y., M.O. and H.N. were involved in the functional studies. A.K. and A.S.-O. performed expression microarray experiments and their analyses. L.-Y.S., D.N., T.A., C.H., F.N., W.-K.H., T.H., H.P.K., T.N., H.M., S. Miyawaki, M.S.-Y., K.I., N.O. and S.C. collected specimens and were involved in project planning. A.K., L.-Y.S., M.M., A.S.-O. and S.O. generated figures and tables. S.O. led the entire project, and A.K. and S.O. wrote the manuscript. All authors participated in the discussion and interpretation of the data.

COMPETING FINANCIAL INTERESTS

The authors declare no competing financial interests.

1. Bejar, R., Levine, R. & Ebert, B.L. Unraveling the molecular pathophysiology of myelodysplastic syndromes. *J. Clin. Oncol.* **29**, 504–515 (2011).
2. Marcucci, G., Haferlach, T. & Dohner, H. Molecular genetics of adult acute myeloid leukemia: prognostic and therapeutic implications. *J. Clin. Oncol.* **29**, 475–486 (2011).
3. Yoshida, K. *et al.* Frequent pathway mutations of splicing machinery in myelodysplasia. *Nature* **478**, 64–69 (2011).
4. Gruber, S., Haering, C.H. & Nasmyth, K. Chromosomal cohesin forms a ring. *Cell* **112**, 765–777 (2003).
5. Nasmyth, K. & Haering, C.H. Cohesin: its roles and mechanisms. *Annu. Rev. Genet.* **43**, 525–558 (2009).
6. Ström, L. *et al.* Postreplicative formation of cohesion is required for repair and induced by a single DNA break. *Science* **317**, 242–245 (2007).
7. Watrin, E. & Peters, J.M. The cohesin complex is required for the DNA damage-induced G2/M checkpoint in mammalian cells. *EMBO J.* **28**, 2625–2635 (2009).
8. Dorsett, D. Cohesin, gene expression and development: lessons from *Drosophila*. *Chromosome Res.* **17**, 185–200 (2009).
9. Dorsett, D. *et al.* Effects of sister chromatid cohesion proteins on cut gene expression during wing development in *Drosophila*. *Development* **132**, 4743–4753 (2005).
10. Horsfield, J.A. *et al.* Cohesin-dependent regulation of Runx genes. *Development* **134**, 2639–2649 (2007).
11. Parelho, V. *et al.* Cohesins functionally associate with CTCF on mammalian chromosome arms. *Cell* **132**, 422–433 (2008).
12. Wendt, K.S. *et al.* Cohesin mediates transcriptional insulation by CCCTC-binding factor. *Nature* **451**, 796–801 (2008).
13. Bose, T. & Gerton, J.L. Cohesinopathies, gene expression, and chromatin organization. *J. Cell Biol.* **189**, 201–210 (2010).
14. Deardorff, M.A. *et al.* HDAC8 mutations in Cornelia de Lange syndrome affect the cohesin acetylation cycle. *Nature* **489**, 313–317 (2012).
15. Deardorff, M.A. *et al.* RAD21 mutations cause a human cohesinopathy. *Am. J. Hum. Genet.* **90**, 1014–1027 (2012).

16. Solomon, D.A. *et al.* Mutational inactivation of STAG2 causes aneuploidy in human cancer. *Science* **333**, 1039–1043 (2011).
17. Beckouët, F. *et al.* An Smc3 acetylation cycle is essential for establishment of sister chromatid cohesion. *Mol. Cell* **39**, 689–699 (2010).
18. Liu, J. *et al.* Transcriptional dysregulation in NIPBL and cohesin mutant human cells. *PLoS Biol.* **7**, e1000119 (2009).
19. Liu, J. *et al.* Genome-wide DNA methylation analysis in cohesin mutant human cell lines. *Nucleic Acids Res.* **38**, 5657–5671 (2010).
20. Schaaf, C.A. *et al.* Regulation of the *Drosophila* enhancer of split and invected-engrailed gene complexes by sister chromatid cohesion proteins. *PLoS ONE* **4**, e6202 (2009).
21. Ding, L. *et al.* Clonal evolution in relapsed acute myeloid leukaemia revealed by whole-genome sequencing. *Nature* **481**, 506–510 (2012).
22. Walter, M.J. *et al.* Clonal architecture of secondary acute myeloid leukemia. *N. Engl. J. Med.* **366**, 1090–1098 (2012).
23. Welch, J.S. *et al.* The origin and evolution of mutations in acute myeloid leukemia. *Cell* **150**, 264–278 (2012).
24. The Cancer Genome Atlas Research Network. Genomic and epigenomic landscapes of adult *de novo* acute myeloid leukemia. *N. Engl. J. Med.* **368**, 2059–2074 (2013).
25. Walter, M.J. *et al.* Clonal diversity of recurrently mutated genes in myelodysplastic syndromes. *Leukemia* **27**, 12785–1282 (2013).
26. Barber, T.D. *et al.* Chromatid cohesion defects may underlie chromosome instability in human colorectal cancers. *Proc. Natl. Acad. Sci. USA* **105**, 3443–3448 (2008).
27. Heidinger-Pauli, J.M., Mert, O., Davenport, C., Guacci, V. & Koshland, D. Systematic reduction of cohesin differentially affects chromosome segregation, condensation, and DNA repair. *Curr. Biol.* **20**, 957–963 (2010).
28. Hadjur, S. *et al.* Cohesins form chromosomal *cis*-interactions at the developmentally regulated IFNG locus. *Nature* **460**, 410–413 (2009).
29. Chan, D.A. & Giaccia, A.J. Harnessing synthetic lethal interactions in anticancer drug discovery. *Nat. Rev. Drug Discov.* **10**, 351–364 (2011).

ONLINE METHODS

Patients and samples. Twenty-nine cases analyzed by whole-exome sequencing were described previously[3]. Anonymized genomic DNA from an additional 581 patients with different myeloid neoplasms were collected from collaborating institutes and used for the analyses described below. All the analyses were performed after written informed consent was obtained. This study was approved by the ethics boards of the University of Tokyo, University Hospital Mannheim, University of Tsukuba, the Munich Leukemia Laboratory, Showa University, Tokyo Metropolitan Ohtsuka Hospital and Chang Gung Memorial Hospital.

Cell lines. The CMS, CMY, UTP-DSAL-1, MOLM-1, MOLM-7, HEL, SS9;22 and TS9;22 cell lines were provided by Y. Hayashi. 293gp and 293gpg cells were provided by R.C. Mulligan. P31FUJ and CMK-86 cells were purchased from the Health Science Research Resources Bank (Osaka, Japan). 293T, KG-1, K562 and F-36P cells were obtained from RIKEN BioResource Center Cell Bank (Tsukuba, Japan), and Kasumi-1, HL-60, MOLM-13 and TF-1 cells were from the American Type Culture Collection. Chromosome spreads were performed for the CMS, Kasumi-1 and MOLM-13 cell lines as previously described[14], except that cells were treated with colcemid (100 μg/ml) and hypotonically swollen in 75 mM KCl for 20 min.

Whole-exome sequencing. The whole-exome sequencing of the 29 paired samples of myelodysplasia was previously described[3], through which we identified a total of 497 candidate single-nucleotide variants and insertions/deletions (indels), of which 268 and 167 were determined by Sanger sequencing as true positives and negatives, respectively, with 62 mutations unconfirmed. In the present study, we updated the list of somatic mutations by rigorously validating the remaining 62 unconfirmed mutations by Sanger sequencing and also by deep sequencing (**Supplementary Table 1**).

Mutation analysis of cohesin components. In total, 534 tumor DNA samples from a variety of myeloid neoplasms were analyzed for possible mutations in nine components of the cohesin complex, *STAG1*, *STAG2*, *SMC1A*, *SMC3*, *RAD21*, *PDS5B*, *ESCO1*, *ESCO2* and *NIPBL*, using high-throughput sequencing of pooled exons amplified from pooled genomic DNA samples. In an additional 47 samples, mutations in *STAG2*, *RAD21*, *SMC1A* and *SMC3* were examined by deep sequencing after enrichment for these targets using a SureSelect custom kit (Agilent) designed to capture all of the coding exons from the target genes, performed as previously described with minor modifications in the algorithm for mutation call[30].

For pooled-DNA sequencing, all target exons (n = 232) encompassing 89,323 nucleotides were PCR amplified using a set of primers having common NotI adaptor sequences on their 5′ ends, digested with NotI, ligated using T4 ligase and sonicated to approximately 200-bp fragments using an ultrasonicator (Covaris); these fragments were used for the generation of sequencing libraries according to a modified pair-end protocol from Illumina. The libraries were then sequenced using HiSeq 2000 (Illumina) with a standard 100-bp paired end–reads protocol. On average, 99.5% of the target bases were analyzed at the depth of 12,000 per pool or 1,000 per sample. Data processing and variant calling were performed as previously described[3] with minor modifications. First, each read from a given DNA pool was aligned to the set of target sequences using BLAT[31] with the -fine option. The mapping information in a .psl format was transformed into a .sam format using the my_psl2sam script, which was further converted into the .bam format using SAMtools[32]. Among the successfully mapped reads, reads were removed from further analysis that either mapped to multiple sites, mapped with more than four mismatched bases or had more than ten clipped bases. Next, the Estimation_CRME script was run to eliminate strand-specific errors and exclude PCR-derived errors. Then, a strand-specific mismatch ratio was calculated for each nucleotide variation for both strands using the bases corresponding to 11–50 cycles. By excluding the top five cycles showing the highest mismatch rates, strand-specific mismatch rates were recalculated, and the smaller value between both strands was adopted as the nominal mismatch ratio. In addition, the nucleotide variations that were present across multiple pools were removed based on permutations across different pools using the Permut_Rm_com script because it is probable that such variations result from systemic sequencing errors. Finally, after excluding variations found in the dbSNP database, the database from the 1000 Genomes project or our in-house SNP database, the variants whose mismatch rate exceeded 0.009 were adopted as candidate mutations. Each candidate mutation was validated by Sanger sequencing of the 12 original individual DNAs from the corresponding DNA pools.

The functional impact of each amino acid substitution was evaluated by computer prediction using SIFT[33], PolyPhen-2 (ref. 34) and Mutation Taster[35]. The significance of nonsilent mutations in each cohesin component was evaluated assuming a uniform distribution of the background mutations within the coding regions, which was estimated to be ~0.3 Mb^{-1} on the basis of a previous whole-exome sequencing of myelodysplasia[3].

Determination of variant allele frequencies. Variant allele frequencies were evaluated by deep sequencing of PCR amplicons, pyrosequencing[36,37] and/or digital PCR (Fluidigm CA, US)[38–40] of the variants using nonamplified DNA. For amplicon sequencing, genomic fragments harboring the variants of interest were PCR amplified using Not1-tagged primers. Ninety-two randomly selected SNP loci that do not contain repetitive sequences were amplified using normal genomic DNA as a template, which served as the control. Touch-down PCRs using high-fidelity DNA polymerase KOD-Plus-Neo (TOYOBO, Tokyo) were performed, and an equimolar mixture of all PCR products was prepared for deep sequencing using HiSeq2000 or Miseq (Illumina), as described above, with a 75-bp or 100-bp pair end–read option. To calculate the allele frequency of each variant, all reads were mapped to the target reference sequence using BLAT[31], followed by differential enumeration of the dichotomic variant alleles. For indels, individual reads were first aligned to each of the wild-type and altered sequences and then assigned to the one with better alignment in terms of the number of matched bases.

Array-based copy-number and methylation analyses. Genomic DNA from 453 bone marrow samples with myeloid neoplasms was analyzed using GeneChip SNP genotyping microarrays as previously described using CNAG/AsCNAR software[41,42]. The results of the SNP array karyotyping for 290 of the 453 cases have been previously published[3,41–44]. The promoter methylation of each cohesin component gene was analyzed using the HumanMethylation450 BeadChip (Illumina), as previously described[30,45], in which methylation status was evaluated by calculating the ratio of methylation-specific and demethylation-specific fluorophores (β value) at each CpG site using iScan software (Illumina).

RT-PCR. Complementary DNA synthesis and quantitative RT-PCR analyses were performed as previously described[3]. The primer sequences used are listed in **Supplementary Tables 16** and **17**.

Protein expression of cohesin components in whole-cell extracts and chromatin-enriched fractions. Whole-cell extracts of myeloid cell lines were separated into soluble supernatant and chromatin-containing pellet fractions and analyzed by SDS-PAGE and protein blot analysis for the expression of different cohesin components as previously described[12,14]. Antibodies used for protein blot analysis are described in **Supplementary Table 18**.

Gene expression and cell proliferation assays. A full-length *RAD21* cDNA (BC050381) was provided by S. Sugano. A full-length *STAG2* cDNA was obtained from total cDNA derived from bone marrow cells and cloned into pBluescript. The truncated mutant of *RAD21* was subcloned by PCR. Flag-tagged *RAD21* or *STAG2* cDNAs were constructed into the retrovirus vector pGCDNsamIRESEGFP (provided by M. Onodera)[46] or a tetracycline-inducible lentiviral vector, CS-TRE-Ubc-tTA-IRESPuro. The wild-type *RAD21*, the mutant *RAD21* and/or a mock-induced retroviral vector were generated as previously described[3] and transduced into Kasumi-1, K562 and TF1 cells, which were sorted by GFP marking using a MoFlo FACS cell sorter (Beckman Coulter) or a BD FACSAria cell sorter (BD Biosciences) 48–96 h after retroviral transduction. The wild-type *RAD21*, the wild-type *STAG2* and a mock-induced lentiviral vector were generated as described previously[47], transduced into MOLM-13 cells and selected by 1 μg/ml puromycin. Gene expression was induced by 1 μg/ml doxcycline. For cell growth assays, the cells were inoculated into 96-well culture plates in RPMI 1640 medium supplemented with 5% FCS (and 5 ng/ml GM-CSF for TF1 cells), and cell growth was monitored in three independent experiments by MTT assay using the Cell Counting Kit-8 (Dojindo Co.).

Expression microarray analysis. RNA was extracted from Kasumi-1 cells that were either mock transduced or transduced with wild-type RAD21 and analyzed in triplicate using the Human Genome U133 Plus 2.0 Array (Affymetrix) according to the manufacturer's protocol. For data analysis, raw array signals were first extracted from .CEL files using dChip Software[48]. After background correction and normalization across the six array data sets, the standardized signal value was obtained for each probe set in each of triplicate array experiments, which were compared between mock-transduced and wild-type *RAD21*-transduced cells. Two independent microarray experiments were performed. To identify transcriptionally altered genes, we used the criteria of fold change greater than ±1.2 and $P < 0.05$ (two-tailed paired t test) in two independent experiments.

RNA sequencing. RNA sequencing of *RAD21*-transduced Kasumi-1 cells and subsequent data analyses were performed as previously described[3] with minor modifications. For quantifications of expression values from the RNA sequencing data, we used a slightly modified version of RKPM (reads per kb of exon per million mapped reads) measures[49]. After removing the sequencing reads that were inappropriately aligned or that had low mapping quality, the number of bases on each exonic region for each RefSeq gene[50] was counted. Then the number of bases was normalized per kb of exon and per 100 million aligned bases. Finally, the expression value of each gene was determined by taking the maximum values among the RefSeq genes corresponding to the gene symbol.

We measured RAD21 expression by differentially enumerating endogenous and exogenous *RAD21* sequence reads, which were discriminated by the absence and presence of the Flag sequence, respectively. After normalization by the number of total reads for each sample, the raw differential read counts were further calibrated against the read counts containing the stop codon in *RAD21*.

Statistical analyses. The significance of the difference in frequency of cohesin component mutations between disease subtypes was tested by one-tailed Fisher's exact test. The coexistence of mutations was tested by two-tailed Fisher's direct method. The significance of the difference in the total number of somatic mutations between cohesin-mutated or -deleted and non-mutated or -deleted samples was tested by Mann-Whitney U test. Differences in the number of numerical abnormalities in cytogenetics between two groups with and without cohesin mutations or deletions was assessed by one-sided χ^2 test.

30. Sato, Y. *et al.* Integrated molecular analysis of clear-cell renal cell carcinoma. *Nat. Genet.* doi:10.1038/ng.2699 (24 June 2013).
31. Kent, W.J. BLAT—the BLAST-like alignment tool. *Genome Res.* **12**, 656–664 (2002).
32. Li, H. *et al.* The Sequence Alignment/Map format and SAMtools. *Bioinformatics* **25**, 2078–2079 (2009).
33. Kumar, P., Henikoff, S. & Ng, P.C. Predicting the effects of coding non-synonymous variants on protein function using the SIFT algorithm. *Nat. Protoc.* **4**, 1073–1081 (2009).
34. Adzhubei, I.A. *et al.* A method and server for predicting damaging missense mutations. *Nat. Methods* **7**, 248–249 (2010).
35. Schwarz, J.M., Rodelsperger, C., Schuelke, M. & Seelow, D. MutationTaster evaluates disease-causing potential of sequence alterations. *Nat. Methods* **7**, 575–576 (2010).
36. Ronaghi, M. Pyrosequencing sheds light on DNA sequencing. *Genome Res.* **11**, 3–11 (2001).
37. Shih, L.Y. *et al.* Emerging kinetics of BCR-ABL1 mutations and their effect on disease outcomes in chronic myeloid leukemia patients with imatinib failure. *Leuk. Res.* **37**, 43–49 (2013).
38. Qin, J., Jones, R.C. & Ramakrishnan, R. Studying copy number variations using a nanofluidic platform. *Nucleic Acids Res.* **36**, e116 (2008).
39. Dube, S., Qin, J. & Ramakrishnan, R. Mathematical analysis of copy number variation in a DNA sample using digital PCR on a nanofluidic device. *PLoS ONE* **3**, e2876 (2008).
40. Totoki, Y. *et al.* High-resolution characterization of a hepatocellular carcinoma genome. *Nat. Genet.* **43**, 464–469 (2011).
41. Nannya, Y. *et al.* A robust algorithm for copy number detection using high-density oligonucleotide single nucleotide polymorphism genotyping arrays. *Cancer Res.* **65**, 6071–6079 (2005).
42. Yamamoto, G. *et al.* Highly sensitive method for genomewide detection of allelic composition in nonpaired, primary tumor specimens by use of affymetrix single-nucleotide-polymorphism genotyping microarrays. *Am. J. Hum. Genet.* **81**, 114–126 (2007).
43. Hosoya, N. *et al.* Genomewide screening of DNA copy number changes in chronic myelogenous leukemia with the use of high-resolution array-based comparative genomic hybridization. *Genes Chromosom. Cancer* **45**, 482–494 (2006).
44. Sanada, M. *et al.* Gain-of-function of mutated C-CBL tumour suppressor in myeloid neoplasms. *Nature* **460**, 904–908 (2009).
45. Nagae, G. *et al.* Tissue-specific demethylation in CpG-poor promoters during cellular differentiation. *Hum. Mol. Genet.* **20**, 2710–2721 (2011).
46. Nabekura, T., Otsu, M., Nagasawa, T., Nakauchi, H. & Onodera, M. Potent vaccine therapy with dendritic cells genetically modified by the gene-silencing–resistant retroviral vector GCDNsap. *Mol. Ther.* **13**, 301–309 (2006).
47. Agarwal, S. *et al.* Isolation, characterization, and genetic complementation of a cellular mutant resistant to retroviral infection. *Proc. Natl. Acad. Sci. USA* **103**, 15933–15938 (2006).
48. Li, C. & Wong, W.H. Model-based analysis of oligonucleotide arrays: expression index computation and outlier detection. *Proc. Natl. Acad. Sci. USA* **98**, 31–36 (2001).
49. Mortazavi, A., Williams, B.A., McCue, K., Schaeffer, L. & Wold, B. Mapping and quantifying mammalian transcriptomes by RNA-Seq. *Nat. Methods* **5**, 621–628 (2008).
50. Pruitt, K.D., Tatusova, T., Brown, G.R. & Maglott, D.R. NCBI Reference Sequences (RefSeq): current status, new features and genome annotation policy. *Nucleic Acids Res.* **40**, D130–D135 (2012).

Int J Hematol (2013) 98:319–322
DOI 10.1007/s12185-013-1418-5

ORIGINAL ARTICLE

Effectiveness and safety of rabbit anti-thymocyte globulin in Japanese patients with aplastic anemia

Tatsuhiro Sakamoto · Naoshi Obara · Naoki Kurita · Mamiko Sakata-Yanagimoto · Hidekazu Nishikii · Yasuhisa Yokoyama · Kazumi Suzukawa · Yuichi Hasegawa · Shigeru Chiba

Received: 4 October 2012 / Revised: 6 August 2013 / Accepted: 6 August 2013 / Published online: 21 August 2013

Abstract Immunosuppressive therapy (IST) with antithymocyte globulin (ATG) and cyclosporine A is the standard treatment for aplastic anemia (AA). The ATG formulation in Japan was changed from horse ATG [Lymphoglobulin® (LG)] to rabbit ATG [Thymoglobulin® (TG)] in 2009. Since then, 12 patients with AA have been treated with TG. Here, we summarize the effectiveness and safety of TG in comparison with data from 14 AA patients treated with LG before April 2009. One subject treated with LG but none treated with TG terminated the treatment due to a grade III adverse effect. The overall 6-month response rate after IST was similar for LG and TG (67 and 75 %). Infection was noted in five (38 %) and four (33 %) subjects treated with LG and TG, respectively. The initial response rate was significantly higher in the early-treatment group treated within a year of diagnosis than in the late-treatment group, who were treated more than a year after diagnosis (85 vs. 29 %, respectively), as reported previously, without apparent differences between the LG and TG groups. We conclude that TG at a dose of 2.5 mg/kg/day for 5 days is effective and safe in Japanese patients with AA.

Keywords ATG · Aplastic anemia · Immunosuppressive therapy

Introduction

Aplastic anemia (AA) is a rare disease pathologically characterized by a fatty bone marrow, in which hematopoietic cells are replaced by fat, resulting in pancytopenia [1]. Patients with severe AA occasionally develop life-threatening infections and experience decreased quality of life due to transfusion dependency and bleeding propensity. Hematopoietic stem cell transplantation is a treatment option. However, it is considered to be the first-line treatment only for young patients with human leukocyte antigen-identical sibling donors because of the high risk of adverse effects.

Immunosuppressive therapy (IST) using anti-thymocyte immunoglobulin (ATG) and cyclosporin A is a standard therapy for patients with moderate-to-severe AA [2–4]. Several ATG formulations that differ in the type of immunogens and immunized animals are available. ATG availability and preferences among practitioners also differ between countries. In Japan, an ATG formulation manufactured from horses [Lymphoglobulin® (LG)] was mainly used since 1995, but was withdrawn from the market in March 2009. Another formulation produced from rabbits [Thymoglobulin® (TG)] replaced LG; thereafter, hematologists have been increasingly incorporating this formulation in their practices without clear treatment guidelines.

Consequently, an optimal TG dose has not been established. A dose of 3.75 mg/kg/day for 5 days is routine in Europe [5], whereas a dose of 2.5 mg/kg/day or 3.75 mg/kg/day for 5 days is recommended by the Pharmaceutical and Medical Devices Agency of Japan.

We reviewed our experience with 12 patients with AA who were treated with TG at a dose of 2.5 mg/kg/day for 5 days at a single center along with our previous data of 14 patients with AA who were treated with LG in order to share our results with other specialists.

T. Sakamoto · N. Obara (✉) · N. Kurita ·
M. Sakata-Yanagimoto · H. Nishikii · Y. Yokoyama ·
K. Suzukawa · Y. Hasegawa · S. Chiba
Department of Hematology, Graduate School of Comprehensive
Human Sciences, University of Tsukuba, Tsukuba,
Ibaraki, Japan
e-mail: n-obara@md.tsukuba.ac.jp

Patients and methods

We reviewed the medical records of 14 patients with AA who treated with LG from January 1997 to April 2009 and 12 patients with AA who were treated with TG from June 2009 to September 2011 at University of Tsukuba Hospital. LG and TG were administered at a dose of 15 mg/kg/day for 5 days and 2.5 mg/kg/day for 5 days, respectively. Cyclosporin A was initiated at a dose of 3 mg/kg every 12 h and continued for at least 6 months at a dose adjusted to maintain trough blood levels at 150–500 ng/ml.

The severity of AA was determined using criteria described by Guinan [6]. Red blood cells and neutrophils with decreased CD59 levels, known as paroxysmal nocturnal hemoglobinuria (PNH)-type blood cells, were detected using flow cytometry based on the method previously reported by Sugimori et al. [7].

Adverse events were evaluated according to the Common Terminology Criteria for Adverse Events version 4.0. If the criteria for febrile neutropenia and detection of causative microbes were fulfilled, the adverse event was classified as an infection.

Treatment responses were defined as follows [8]: complete response (CR) in any AA type with absolute neutrophil count $> 2.0 \times 10^9$/L, hemoglobin levels > 11 g/dL, and platelet count $> 100 \times 10^9$/L; partial response (PR) in severe AA with an improvement in blood counts no longer satisfying the criteria for severe AA but insufficient to meet the criteria for CR; and PR in nonsevere AA with transfusion independence (if previously transfusion-dependent), doubling or normalization of at least 1 cell line, or an increase above baseline in at least 1 cell line in hemoglobin by 3 g/dL (if initially < 6 g/dL), increase in neutrophil count by 500/μL (if initially < 500), or increase in platelet count by 20000/μL (if initially < 20000). Overall response included both CR and PR. Responses were determined by evaluating peripheral blood counts at 3, 6, and 12 months after initiating IST. Statistical analysis was conducted based on a group sequential trial design, using a 2-sided test at a 5 % significance level, 80 % power, and 1 interim analysis.

Results

There were no significant differences between the subjects in the LG- and TG-treated groups in terms of age, gender, disease severity, complications, time from diagnosis to the start of treatment, or the of positive PNH-type blood cells (Table 1). IST using LG had previously been employed in 1 of 14 subjects in the LH-treated group and 4 of 12 subjects in the TG-treated group. Treatments were administered within a year of the diagnosis in 8 of 14 subjects treated with LG and in 7 out of 12 subjects treated with TG. The median period of observation was 50 and 19 months in the LG- and TG-treated groups, respectively. The TG-treated group included 4 patients who received TG as a second course of ATG treatment because of AA relapse.

Of all treatment-induced adverse events (Table 2), the most common was fever. Abnormal liver function was also observed in 1 subject treated with LG, leading to termination of treatment. All the other subjects completed the ATG treatment. Infection was documented in 9 subjects; 4

Table 1 Patients' characteristics

Patient	LG	TG
Number	14	12
Median age (range)	50 (27–77)	54 (22–73)
Male:Female	7:7	7:5
Term	1997–2009	2009–2011
Disease status		
Severe	6	6
Non-severe	8	6
Time from diagnosis		
Median, day (range)	2453 (6–6746)	3025 (10–6455)
3 months	5	3
3–12 months	3	4
12 months	6	5
Times of ATG therapy		
First ATG	14	8
Second ATG	1	4
PNH clone		
Positive	6	6
Negative	1	6
Unexamined	7	0

LG horse ATG [Lymphoglobulin® (LG)], *TG* rabbit ATG [Thymoglobulin® (TG)]

Table 2 Adverse events

	LG ($n = 14$)	TG ($n = 12$)
Fever at administration		
Yes	7	4
No	7	8
Serum disease		
Yes	0	0
No	14	12
Liver injury		
Yes	1	0
No	13	12
Infection		
Yes	5	4
No	9	8

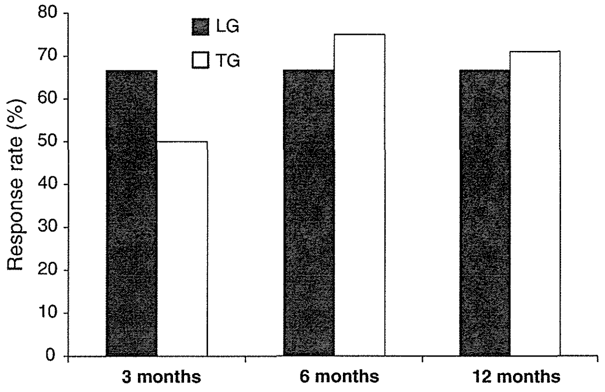

Fig. 1 Overall response to TG and LG at 3, 6, and 12 months

in the TG- and 5 in the LG-treated groups, respectively. Intravenous antibiotics were prescribed for all subjects. Cytomegalovirus infection was observed in 1 subject treated with TG. Although periodic inspection was not carried out in a complete manner, the EBV-related lymphoproliferative disorders were not detected in either group.

Because the relapsed patients were more likely to respond to the second course of ATG treatment, we analyzed these patients separately for overall response. The overall 6-month response rate after ATG administration was 67 % (8 of 12 subjects) with LG and 75 % (6 of 8 subjects) with TG (Fig. 1). Responses were observed after 3 months in 67 and 50 % subjects in the LG- and TG-treated groups, respectively. One subject treated with TG showed a response after 6 months, suggesting the possibility of a late response. A significant difference in the response rate was not detected between both groups.

In the similar evaluations only after the first ATG, the response rate at 6 months from ATG treatment in patients with severe AA (16 subjects) appeared to be higher than that in patients with non-severe AA [4 subjects (75 vs. 50 %)], although not statistically significant. The response rates tended to be higher in subjects treated with LG or TG earlier *after diagnosis than those in subjects treated later.* Treatment with LG and TG in 7 and 6 subjects, respectively, was initiated within a year of diagnosis (early treatment group), whereas treatment with LG and TG in the remaining 5 and 2 subjects, respectively, was initiated more than 1 year after diagnosis (late treatment group). Response rate after 6 months from ATG treatment was achieved more rapidly in the early treatment group than in the late treatment group (85 and 29 %, respectively; $p = 0.005$).

Again with the evaluations of the first ATG, the response rate at 6 months from ATG treatment tended to be higher in subjects with PNH-type blood cells (10 subjects) than in those without PNH-type blood cells (4 subjects), although the difference was not statistically significant (PNH-type cells positive and negative in 9 and 4 subjects, 70 and 50 %, respectively; $p = 0.63$).

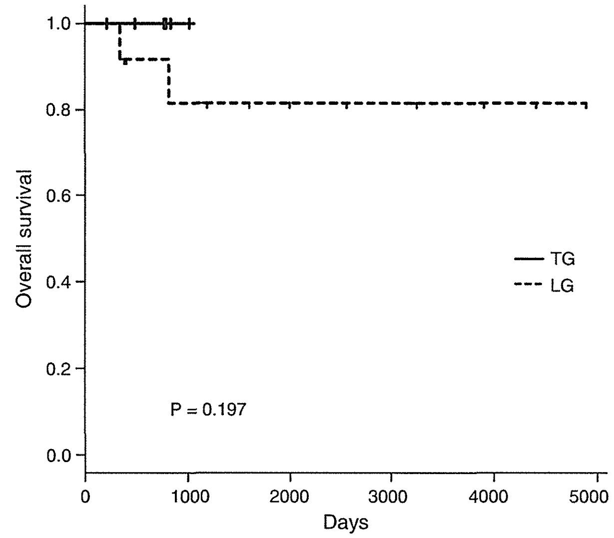

Fig. 2 Overall survival curves $p = 0.197$

With regard to the overall survival curves, no significant difference was detected between both groups, although the number of subjects is small (Fig. 2).

Discussion

We described the effectiveness and safety of TG in a small number of Japanese patients with AA. A recent multicenter prospective study comparing LG and TG in European countries demonstrated that LG was more effective than TG, with both formulations having a similar safety profile [9]. Another multicenter prospective randomized study in the US showed that horse ATG [ATGAM®] was more effective than TG [10].

Nevertheless, the availability of ATG formulations differs between countries [11]. The decision to change the ATG formulation in Japan was made by providers based on the similar efficacy of TG and LG in the second course of ATG treatment for patients who failed to respond to the first course with LG [12].

Given that ATG formulations differ between countries, it is necessary to perform a direct comparison between LG and TG in other ethnic groups in the Asia. A recent single-center retrospective study from Korea comparing LG and TG demonstrated that the overall survival rate and failure-free survival rate were not significantly different between the two groups, but failure-free survival rate tended to be higher in TG group [13, 14].

A prerequisite to that, however, is the dose adjustment of each formulation. For TG, the advantage of a dose of

3.75 mg/kg/day for 5 days over 2.5 mg/kg/day for 5 days was demonstrated in a European clinical study. However, a dose of 2.5 mg/kg/day or 3.75 mg/kg/day for 5 days is recommended in Japan because of insufficient evidence regarding an optimal dose [9, 15].

These circumstances embarrass hematologists who treat patients with AA in Japan, and thus, we need to share our experiences of treating this rare disease with TG. Given the lack of safety data, an initial dose of 2.5 mg/kg/day for 5 days was chosen to treat the 12 patients with AA. The response rate of 63 % was within our expectation or could exceed it, given the fact that the treatment with TG in the second course of IST in 4 of 12 subjects exceeded our expectation. The response rate was 56 % in 13 subjects treated with LG, suggesting that the effectiveness of TG at a dose of 2.5 mg/kg or LG at a dose of 15 mg/kg for 5 days is not substantially different. Adverse effects with TG formulations, such as infections, were also similar to those with LG formulations at these doses.

When the 26 subjects treated with LG or TG were analyzed together, we confirmed that the period from the diagnosis to the start of IST is a statistically significant predictor of the efficacy of IST, as reported previously [4, 16, 17]. We also observed a trend suggesting that the presence of PNH-type blood cells is an indicator of higher IST effectiveness in the same patient cohort, as reported previously [6, 18].

Based on these encouraging observations, we have increased the dose of TG from 2.5 to 3.75 mg/kg/day for 5 days in the current prescription for our patients with AA, expecting better responses without increasing the risk of adverse events. These small efforts may help us design future clinical trials of ATG-based IST for AA, not only in Japan but also throughout Asia.

References

1. Young NS, Calado RT, Scheinberg P. Current concepts in the pathophysiology and treatment of aplastic anemia. Blood. 2006;108:2509–19.
2. Kojima S, Nakao S, Young N, Bacigalupo A, Gerard G, Hirano N, et al. The Third Consensus Conference on the treatment of aplastic anemia. Int J Hematol. 2011;93:832–7.
3. Frickhofen N, Heimpel H, Kaltwasser JP, Schrezenmeier H. Antithymocyte globulin with or without cyclosporin A: 11-year follow-up of a randomized trial comparing treatments of aplastic anemia. Blood. 2003;101:1236–42.
4. Locasciulli A, Oneto R, Bacigalupo A, Socié G, Korthof E, Bekassy A, et al. Outcome of patients with acquired aplastic anemia given first line bone marrow transplantation or immunosuppressive treatment in the last decade: a report from the European Group for Blood and Marrow Transplantation (EBMT). Haematologica. 2007;92:11–8.
5. Marsh JC, Ball SE, Cavenagh J, Darbyshire P, Dokal I, Gordon-Smith EC, et al. Guidelines for the diagnosis and management of aplastic anaemia. Br J Haematol. 2009;147:43–70.
6. Guinan EC. Diagnosis and management of aplastic anemia. Hematol Am Soc Hematol Educ Program. 2011; 76–81.
7. Sugimori C, Chuhjo T, Feng X, Yamazaki H, Takami A, Teramura M, et al. Minor population of CD55–CD59- blood cells predicts response to immunosuppressive therapy and prognosis in patients with aplastic anemia. Blood. 2006;107:1308–14.
8. Camitta BM. What is the definition of cure for aplastic anemia? Acta Haematol. 2000;103:16–8.
9. Marsh JC, Bacigalupo A, Schrezenmeier H, Tichelli A, Risitano AM, et al. Prospective study of rabbit antithymocyte globulin and cyclosporine for aplastic anemia from the EBMT Severe Aplastic Anemia Working Party. Blood. 2012;119:5391–6.
10. Scheinberg P, Nunez O, Weinstein B, Scheinberg P, Biancotto A, Wu CO, et al. Horse versus rabbit antithymocyte globulin in acquired aplastic anemia. N Engl J Med. 2011;365:430–8.
11. Afable MG, Shaik M, Sugimoto Y, Elson P, Clemente M, Makishima H, et al. Efficacy of rabbit anti-thymocyte globulin in severe aplastic anemia. Haematologica. 2011;96:1269–75.
12. Scheinberg P, Nunez O, Young NS. Retreatment with rabbit anti-thymocyte globulin and cyclosporine for patients with relapsed or refractory severe aplastic anemia. Br J Haematol. 2006;133: 622–7.
13. Shin SH, Lee JW. The optimal immunosuppressive therapy for aplastic anemia. Int J Hematol. 2013;97:564–72.
14. Shin SH, Yoon JH, Yahung SA, Lee SE, Cho BS, Eom KS, et al. The efficacy of rabbit antithymocyte globulin with cyclosporine in comparison to horse antithymocyte globulin as a first-line treatment in adult patients with severe aplastic anemia: a single-center retrospective study. Ann Hematol. 2013;92:817–24.
15. Di Bona E, Rodeghiero F, Bruno B, Gabbas A, Fao Po, et al. Rabbit antithymocyte globulin (r-ATG) plus cyclosporine and granulocyte colony stimulating factor is an effective treatment for aplastic anaemia patients unresponsive to a first course of intensive immunosuppressive therapy. Gruppo Italiano Trapianto di Midollo Osseo (GITMO). Br J Haematol. 1999;107:330–4.
16. Scheinberg P, Nunez O, Young NS. Retreatment with rabbit anti-thymocyte globulin and cyclosporine for patients with relapsed or refractory severe aplastic anaemia. Br J Haematol. 2006;133: 622–7.
17. Stadler M, Germing U, Kliche KO, Josten KM, Kuse R, Hofmann WK, et al. A prospective, randomised, phase II study of horse antithymocyte globulin vs rabbit antithymocyte globulin as immune-modulating therapy in patients with low-risk myelodysplastic syndromes. Leukemia. 2004;18:460–5.
18. Nakao S, Sugimori C, Yamazaki H. Clinical significance of a small population of paroxysmal nocturnal hemoglobinuria-type cells in the management of bone marrow failure. Int J Hematol. 2006;84:118–22.

nature genetics

Somatic *RHOA* mutation in angioimmunoblastic T cell lymphoma

Mamiko Sakata-Yanagimoto[1,22], Terukazu Enami[1,22], Kenichi Yoshida[2,3,22], Yuichi Shiraishi[4], Ryohei Ishii[5], Yasuyuki Miyake[1], Hideharu Muto[1], Naoko Tsuyama[6], Aiko Sato-Otsubo[2,3], Yusuke Okuno[2], Seiji Sakata[7], Yuhei Kamada[1], Rie Nakamoto-Matsubara[1], Nguyen Bich Tran[1], Koji Izutsu[8,9], Yusuke Sato[2,3], Yasunori Ohta[10], Junichi Furuta[11], Seiichi Shimizu[12], Takuya Komeno[13], Yuji Sato[14], Takayoshi Ito[15], Masayuki Noguchi[16], Emiko Noguchi[17], Masashi Sanada[2,3], Kenichi Chiba[4], Hiroko Tanaka[18], Kazumi Suzukawa[1,19], Toru Nanmoku[19], Yuichi Hasegawa[1], Osamu Nureki[5], Satoru Miyano[4,18], Naoya Nakamura[20], Kengo Takeuchi[6,7], Seishi Ogawa[2,3,23] & Shigeru Chiba[1,21,23]

Angioimmunoblastic T cell lymphoma (AITL) is a distinct subtype of peripheral T cell lymphoma characterized by generalized lymphadenopathy and frequent autoimmune-like manifestations[1,2]. Although frequent mutations in *TET2, IDH2* and *DNMT3A,* which are common to various hematologic malignancies[3,4], have been identified in AITL[5–8], the molecular pathogenesis specific to this lymphoma subtype is unknown. Here we report somatic *RHOA* mutations encoding a p.Gly17Val alteration in 68% of AITL samples. Remarkably, all cases with the mutation encoding p.Gly17Val also had *TET2* mutations. The *RHOA* mutation encoding p.Gly17Val was specifically identified in tumor cells, whereas *TET2* mutations were found in both tumor cells and non-tumor hematopoietic cells. *RHOA* encodes a small GTPase that regulates diverse biological processes. We demonstrated that the Gly17Val RHOA mutant did not bind GTP and also inhibited wild-type RHOA function. Our findings suggest that impaired RHOA function in cooperation with preceding loss of TET2 function contributes to AITL-specific pathogenesis.

AITL accounts for approximately 20% of all T cell lymphoma cases[1]. On the basis of gene expression profiling, the normal counterparts of AITL tumor cells are proposed to be follicular helper T cells (T_{FH} cells), a subset of helper T cells[1,2]. Peripheral T cell lymphoma, not otherwise specified (PTCL-NOS) represents a more heterogeneous category of mature T cell lymphomas, including a subset sharing some features of AITL[5,9].

To explore the relevant gene mutations responsible for the pathogenesis of AITL, we performed whole-exome sequencing[10] of three AITL and three PTCL-NOS samples (**Supplementary Table 1**). Of the targeted sequence, 86.5% was analyzed by ≥20 independent reads on average (**Supplementary Figs. 1** and **2**). In total, we identified and confirmed 87 non-silent somatic mutations (4–27 (median of 12.5) per sample) by Sanger sequencing and/or deep sequencing (**Fig. 1a** and **Supplementary Table 2**), including 79 missense and 5 nonsense single-nucleotide variants (SNVs) and 1 non-frameshift and 2 frameshift deletions. The numbers of non-silent mutations were lower than reported in B cell neoplasms[11,12], although relatively low tumor contents, which were suspected owing to mutant allele frequencies of generally less than 0.25 (median of 0.11), could have compromised sensitivity in detecting mutations (**Fig. 1a**). Recurrent mutations were found in only one gene, *RHOA*, in which identical c.50G>T mutations predicted to result in a p.Gly17Val alteration were identified in one PTCL-NOS and three AITL specimens (**Fig. 1a,b** and **Supplementary Fig. 3**). No allelic imbalances were observed at the *RHOA* locus (**Supplementary Fig. 4**).

Prompted by this discovery, we screened *RHOA* mutations in an extended cohort of 72 AITL and 87 PTCL-NOS samples by

---

[1]Department of Hematology, Faculty of Medicine, University of Tsukuba, Tsukuba, Japan. [2]Cancer Genomics Project, Graduate School of Medicine, The University of Tokyo, Tokyo, Japan. [3]Department of Pathology and Tumor Biology, Graduate School of Medicine, Kyoto University, Kyoto, Japan. [4]Laboratory of DNA Information Analysis, Human Genome Center, Institute of Medical Science, The University of Tokyo, Tokyo, Japan. [5]Department of Biophysics and Biochemistry, Graduate School of Science, The University of Tokyo, Tokyo, Japan. [6]Division of Pathology, Cancer Institute, Japanese Foundation for Cancer Research, Tokyo, Japan. [7]Pathology Project for Molecular Targets, Cancer Institute, Japanese Foundation for Cancer Research, Tokyo, Japan. [8]Department of Hematology, Toranomon Hospital, Tokyo, Japan. [9]Okinaka Memorial Institute for Medical Research, Tokyo, Japan. [10]Department of Pathology, Toranomon Hospital, Tokyo, Japan. [11]Department of Dermatology, Faculty of Medicine, University of Tsukuba, Tsukuba, Japan. [12]Department of Hematology, Tsuchiura Kyodo General Hospital, Tsuchiura, Japan. [13]Department of Hematology, Mito Medical Center, National Hospital Organization, Mito, Japan. [14]Department of Hematology, Tsukuba Memorial Hospital, Tsukuba, Japan. [15]Department of Hematology, JA Toride Medical Center, Toride, Japan. [16]Department of Pathology, Faculty of Medicine, University of Tsukuba, Tsukuba, Japan. [17]Department of Medical Genetics, Faculty of Medicine, University of Tsukuba, Tsukuba, Japan. [18]Laboratory of Sequence Analysis, Human Genome Center, Institute of Medical Science, The University of Tokyo, Tokyo, Japan. [19]Department of Clinical Laboratory, University of Tsukuba Hospital, Tsukuba, Japan. [20]Department of Pathology, Tokai University School of Medicine, Isehara, Japan. [21]Life Science Center, Tsukuba Advanced Research Alliance, University of Tsukuba, Tsukuba, Japan. [22]These authors contributed equally to this work. [23]These authors jointly directed this work. Correspondence should be addressed to S.C. (schiba-t@md.tsukuba.ac.jp) or S.O. (sogawa-tky@umin.ac.jp).

Received 13 May 2013; accepted 12 December 2013; published online 12 January 2014; doi:10.1038/ng.2872

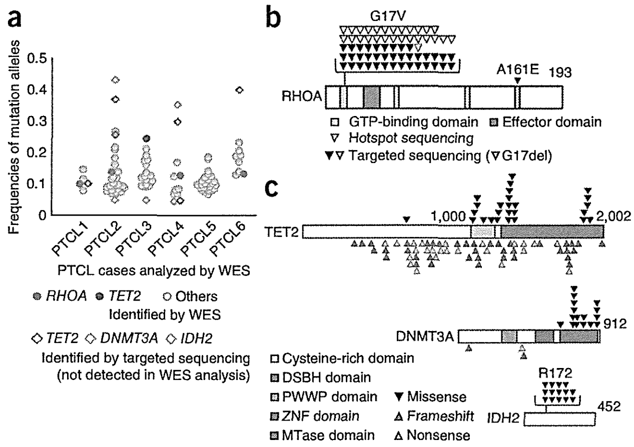

Figure 1 Discovery of a *RHOA* mutation encoding p.Gly17Val in PTCL by whole-exome sequencing. (**a**) Somatic mutations identified in three AITL and three PTCL-NOS samples are shown with the frequencies of mutation alleles plotted. Red and blue filled circles indicate the *RHOA* mutation encoding p.Gly17Val and *TET2* mutations, respectively. Mutations of *TET2*, *IDH2* and *DNMT3A* that were not found by whole-exome sequencing (WES) but were identified later by targeted deep sequencing are also depicted by open diamonds: blue, *TET2*; orange, *DNMT3A*; purple, *IDH2*. (**b**) Positions of RHOA alterations. Nucleotide-binding domains are represented by yellow boxes. The effector domain is represented by a red box. (**c**) Positions of alterations in the TET2, DNMT3A and IDH2 proteins. Black, red and yellow arrowheads indicate missense, frameshift and nonsense mutations, respectively. The cysteine-rich and double-strand β-helix (DSBH) domains of TET2 are represented by a yellow and a red box, respectively. proline-tryptophan-tryptophan-proline (PWWP), zinc-finger (ZNF) and methyltransferase (MTase) domains of DNMT3A are shown by light blue, blue and purple boxes, respectively.

deep sequencing of all coding sequences ($n = 79$) or the mutational hotspot (c.50G>T; p.Gly17Val) ($n = 80$) of *RHOA* (**Supplementary Fig. 1** and **Supplementary Table 3**). *RHOA* mutations were found in 66 of the 159 specimens, with a much higher frequency in AITL (51/72; 70.8%) than PCTL-NOS (15/87; 17.2%) (**Fig. 1b**, **Table 1** and **Supplementary Table 4**). We identified no *RHOA* mutations other than the c.50G>T (p.Gly17Val) mutation except for an in-frame deletion (c.49_51delGGA) resulting in a p.Gly17del (PTCL33) alteration and a missense SNV (c.482C>A) resulting in a p.Ala161Glu (PTCL59) alteration in cases negative for the p.Gly17Val alteration (**Fig. 1b** and **Supplementary Table 4**). We validated all low-frequency mutant *RHOA* alleles (frequency of 0.02–0.05) using an independent deep sequencing platform (Online Methods). No *RHOA* mutations encoding p.Gly17Val were found in other hematologic malignancies, including in myeloid neoplasms ($n = 142$), mature B cell neoplasms ($n = 91$) and mature T cell neoplasms other than AITL and PTCL-NOS ($n = 11$) (**Table 1**), suggesting that the *RHOA* mutation encoding p.Gly17Val is highly specific to AITL and PTCL-NOS among hematologic malignancies.

According to the pathologic definition in the Online Methods[5,9], we classified 21 of 59 immunohistochemically characterized PTCL-NOS cases as T_{FH}-like PTCL-NOS cases. Thirteen of the 21 T_{FH}-like PTCL-NOS cases (61.9%) had the *RHOA* mutation encoding p.Gly17Val, whereas none of the remaining 38 PTCL-NOS cases had this mutation ($P < 0.001$) (**Supplementary Table 5**). Given that almost all AITL cases showed T_{FH}-like features, these findings implied a strong correlation between the *RHOA* mutation encoding p.Gly17Val and the T_{FH}-like phenotype of PTCL, similar to the correlation previously shown between *TET2* mutations and the T_{FH}-like phenotype of PTCL[5]. No clinical parameters were significantly different in the mutation-positive and mutation-negative cases (**Supplementary Fig. 5** and **Supplementary Table 6**).

To investigate the correlation between mutations in *RHOA* and other genes, we also resequenced *TET2*, *IDH1*, *IDH2* and *DNMT3A* in addition to *RHOA* in the subcohort of 79 PTCL (AITL, 46; PTCL-NOS, 33) cases (**Supplementary Figs. 1** and **6**). A total of 97 *TET2* mutations were identified in 54 of the 79 PTCL specimens (68.4%) (AITL, 38 (82.6%); PTCL-NOS, 16 (48.5%)). Similarly, we found *DNMT3A* mutations in 21 PTCL specimens (26.6%) (AITL, 12 (26.0%); PTCL-NOS, 9 (27.3%)). We identified *IDH2* mutations affecting Arg172 (p.Arg172Met, p.Arg172Thr, p.Arg172Ser, p.Arg172Lys and p.Arg172Gly) in 14 cases (17.7%) (AITL, 14 (30.4%); PTCL-NOS, 0 (0%)) (**Figs. 1c** and **2a**, **Supplementary Tables 7** and **8**, and **Supplementary Note**). No *IDH1* mutations were identified. Several mutations in *TET2*, *IDH2* and *DNMT3A*, which had escaped detection in the whole-exome sequencing analysis, were newly identified in the same whole-exome sequencing cohort by this targeted resequencing. Our inability to detect these mutations using whole-exome sequencing might be explained by their low allelic mutational burdens and/or by low sequencing coverage in whole-exome sequencing (**Fig. 1a**). Unexpectedly, however, *TET2* and *DNMT3A* mutations with high-frequency alleles were also newly found in three and two cases, respectively (**Fig. 1a**). The cause of our inability to identify *TET2* and *DNMT3A* mutations by whole-exome sequencing might be the presence of substantial numbers of mutant reads in the reference bone marrow samples (**Supplementary Fig. 7**, **Supplementary Tables 9** and **10**, and **Supplementary Note**).

Remarkably, mutations in *RHOA*, *TET2* and *IDH2* showed strong correlations; all *RHOA*-mutated cases also had *TET2* mutations ($P < 0.001$), and all but one of the *IDH2* mutations were confined to tumors also having *RHOA* and *TET2* mutations ($P < 0.001$) (**Fig. 2a** and **Supplementary Note**). The predominant *TET2* alleles showed significantly higher allelic burden than mutant *RHOA* and *IDH2* alleles in most cases (*TET2* versus *RHOA*, $P < 0.001$; *TET2* versus *IDH2*, $P = 0.001$; **Fig. 2b,c**), whereas *RHOA* and *IDH2* mutations had similar allele frequencies (**Fig. 2d**). Skewed distributions of relative allele frequencies among these mutations strongly suggested that *TET2* mutations predated *RHOA* and/or *IDH2* mutations in most cases.

Table 1 ***RHOA* mutation encoding p.Gly17Val in various hematologic malignancies**

Disease	Number of mutated cases (%)
T cell malignancies	$n = 170$
AITL[a]	51/72 (70.8)
PTCL-NOS	15/87 (17.2)
with AITL features	13/21 (61.9)
without AITL features	0/38 (0)
ND[b]	2/28 (7.1)
Other T cell malignancies	0/11 (0)
B cell malignancies	$n = 91$
DLBCL	0/44 (0)
Follicular lymphoma	0/19 (0)
Other B cell malignancies	0/28 (0)
Myeloid malignancies	$n = 142$
AML	0/89 (0)
MDS	0/36 (0)
MPN	0/14 (0)
MDS/MPN	0/3 (0)

DLBCL, diffuse large B cell lymphoma; AML, acute myeloid leukemia; MDS, myelodysplastic syndrome; MPN, myeloproliferative neoplasm.
[a] Including one case with RHOA p.Gly17del and one case with RHOA p.Ala161Glu.
[b] Not determined.

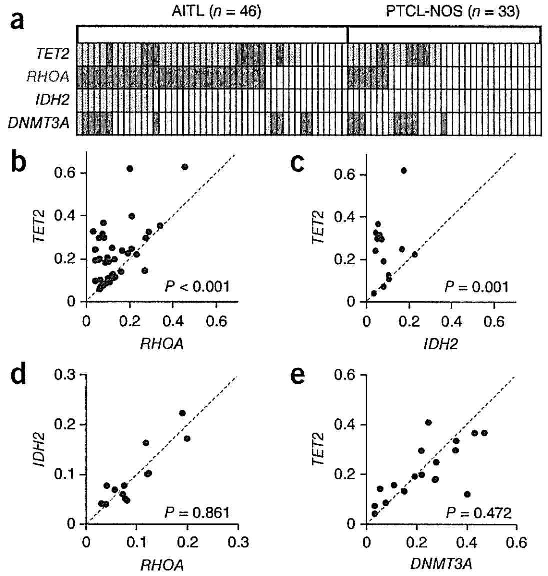

Figure 2 Relationship between *RHOA*, *TET2*, *IDH2* and *DNMT3A* mutations in PTCL. (**a**) Distribution of mutations in *RHOA*, *TET2*, *IDH2* and *DNMT3A* in 79 PTCL (46 AITL and 33 PTCL-NOS) samples that were analyzed by targeted deep sequencing. Two or three distinct *TET2* mutations and two distinct *DNMT3A* mutations were identified in multiple samples. Dark blue and dark green indicate samples having a single *TET2* or *DNMT3A* mutation, respectively, and light blue and light green indicate samples having multiple *TET2* or *DNMT3A* mutations. (**b**–**e**) Comparison of the allele frequencies of two selected mutations in samples harboring mutations in *TET2* and *RHOA* (**b**), *TET2* and *IDH2* (**c**), *RHOA* and *IDH2* (**d**) and *TET2* and *DNMT3A* (**e**). Each axis shows the frequencies of the mutant alleles. When multiple mutations existed in a single gene, the frequencies of major alleles are indicated. Data were analyzed statistically by Wilcoxon rank-sum test.

Mutations in *DNMT3A* largely overlapped and had similar allelic burdens as *TET2* mutations (**Fig. 2e**), but their correlation with *RHOA* or *IDH2* mutations was much less clear (**Fig. 2a**).

To determine the clonal structure of the *RHOA* mutation encoding p.Gly17Val and of other gene mutations, we isolated CD4$^+$ T cells, a fraction enriched for tumor cells and other fractions, from the specimens of two cases (PTCL159 and PTCL160; **Supplementary Figs. 8** and **9**), and we analyzed mutations by targeted resequencing as well as by Sanger sequencing. In PTCL159 (PTCL-NOS in the skin), we found the *RHOA* mutation encoding p.Gly17Val, two *TET2* mutations and a *DNMT3A* mutation (**Supplementary Fig. 8** and **Supplementary Table 7**). Somatic origin of these mutations was confirmed (**Supplementary Fig. 8**). We identified the *RHOA* mutation encoding p.Gly17Val in purified CD4$^+$ cells but not in CD8$^+$ cells. One of the two *TET2* mutations and the *DNMT3A* mutation were identified in both CD4$^+$ and CD8$^+$ cell fractions with apparently similar allelic burdens to each other in the two types of cells, whereas the remaining *TET2* mutation was found only in CD4$^+$ cells and was absent in CD8$^+$ cells (**Supplementary Fig. 8**). These observations suggested that the *RHOA* mutation encoding p.Gly17Val and one of the two *TET2* mutations were confined to CD4$^+$ tumor cells, whereas the other *TET2* mutation and the *DNMT3A* mutation were shared by both CD4$^+$ tumor cells and CD4$^+$ and CD8$^+$ reactive cells (**Supplementary Fig. 8**). In contrast, the *RHOA* mutation encoding p.Gly17Val and two *TET2* mutations identified in PTCL160 (AITL) were all confined to tumor cells (**Supplementary Fig. 9**, **Supplementary Table 7** and **Supplementary Note**). These data indicate that the *RHOA* mutation encoding p.Gly17Val was a specific event in tumor cells. In contrast, *TET2* and *DNMT3A* mutations seemed to have taken place in either CD4$^+$ tumor cells or early progenitor cells such as those that give rise to all hematopoietic cells, as previously described[6,7].

RHOA encodes a small GTPase, which has a highly conserved amino acid structure across species (**Supplementary Fig. 10**). RHOA operates as a molecular switch that regulates a wide variety of biological processes through cycling between an active (GTP-bound) state and an inactive (GDP-bound) state[13,14]. RHOA is activated by specific guanine-exchange factors (GEFs) that catalyze the dissociation of GDP and the rebinding of GTP, and signaling is terminated by hydrolysis of GTP to GDP, a reaction that is stimulated by GTPase-activating proteins (GAPs)[13,14].

Three-dimensional model structures of the Gly17Val RHOA protein suggest compromised binding to GDP and GTP[15,16] (**Supplementary Fig. 11** and **Supplementary Note**). In fact, when we expressed RHOA proteins in NIH3T3 cells, a substantial fraction of wild-type RHOA protein bound GTP or GTPγS in a rhotekin pulldown assay[17], whereas no GTP- or GTPγS-bound form was pulled down for the Gly17Val RHOA mutant (**Fig. 3a**), suggesting severely reduced GTP and GTPγS binding by the Gly17Val mutant.

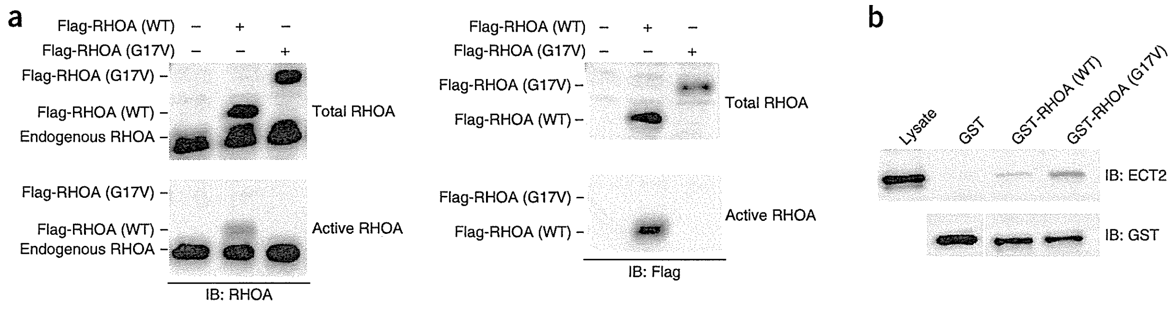

Figure 3 Dominant-negative effect of the Gly17Val RHOA mutant on wild-type RHOA. (**a**) Rhotekin pulldown assay for endogenous RHOA and exogenously expressed wild-type and Gly17Val RHOA in NIH3T3 cells. Extracts from NIH3T3 cells expressing Flag-tagged wild-type or Gly17Val RHOA were pulsed with GTPγS and incubated with glutathione Sepharose beads on which the RHO-binding domain of rhotekin fused to GST was immobilized, and precipitated protein was blotted with antibodies to RHOA (left) and Flag (right) to detect active RHOA specifically. IB, immunoblot; WT, wild type. (**b**) GEF-binding activity of wild-type and Gly17Val RHOA. Lysate from NIH3T3 cells, transiently expressing ECT2 with an N-terminal deletion, was incubated with Sepharose beads on which GST-fused wild-type or Gly17Val RHOA protein was immobilized, and precipitated protein was blotted with antibody to ECT2.

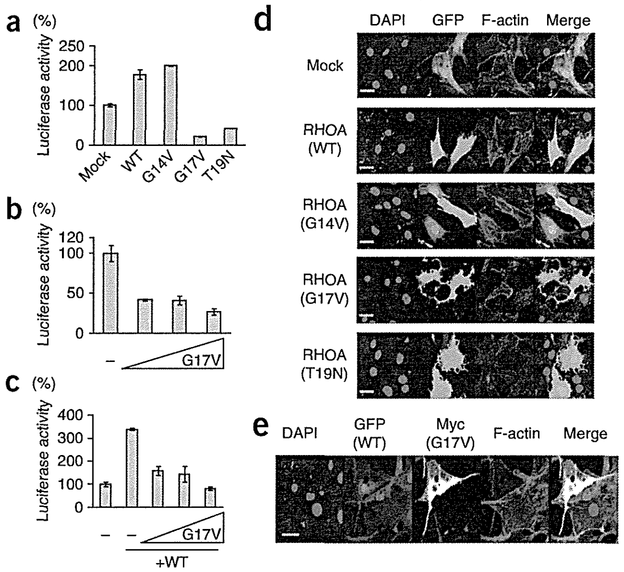

Figure 4 Effects of the Gly17Val RHOA mutant on transcriptional regulation and actin cytoskeleton formation in NIH3T3 cells. (**a–c**) Effect of Gly17Val RHOA on the transcriptional activity of the SRF-RE. (**a**) Activity of the SRF-RE reporter in NIH3T3 cells expressing wild-type or mutant (Gly14Val, Gly17Val or Thr19Asn) RHOA protein. (**b**) Effect of increasing amounts (16, 48 or 144 ng/well) of Gly17Val RHOA on SRF-RE reporter activity in NIH3T3 cells. (**c**) Effect of increasing amounts (16, 48 or 144 ng/well) of Gly17Val RHOA on SRF-RE reporter activity enhanced by exogenously expressed wild-type RHOA. In each plot in **a**–**c**, the mean ± s.d. of triplicate experiments is shown. A representative result from three independent experiments is shown. (**d**,**e**) Effect of Gly17Val RHOA on actin cytoskeleton formation. (**d**) F-actin staining with phalloidin (red) in NIH3T3 cells transiently transfected with vector expressing wild-type or mutant (Gly14Val, Gly17Val or Thr19Asn) RHOA. GFP is used as a marker for transduction with each cDNA. (**e**) NIH3T3 cells stably expressing wild-type RHOA were transfected with vector expressing Myc-tagged Gly17Val RHOA. Scale bars in **d**,**e**, 30 μm.

Moreover, the Gly17Val RHOA mutant reduced GTP binding by both the endogenous and exogenous wild-type RHOA proteins in a dose-dependent manner (**Supplementary Figs. 12** and **13**), suggesting a dominant-negative nature for Gly17Val RHOA. This view was further supported by the finding that the Gly17Val RHOA mutant bound ECT2, one of the RhoGEFs, more tightly than wild-type RHOA, as was previously described for Gly17Ala RHOA[18] (**Fig. 3b** and **Supplementary Note**). The Gly17del and Ala161Glu mutants also showed impaired binding capacity for GTP/GTPγS and inhibited GTP binding by wild-type RHOA protein (**Supplementary Fig. 14**). Together, these results support the notion that the RHOA mutants contribute to the pathogenesis of PTCL through the inhibition of wild-type RHOA in a dominant-negative manner, although the amount of mutant RHOA protein seemed to be low in both NIH3T3 cells and primary AITL tumor cells (**Supplementary Fig. 15**, **Supplementary Table 11** and **Supplementary Note**), for an unknown reason.

In accordance with these findings, unlike wild-type RHOA and mutant Gly14Val RHOA, the Gly17Val RHOA mutant did not activate transcription from the serum response factor–responsive element (SRF-RE)[19] (**Fig. 4a**,**b**) and instead repressed transcription from SRF-RE activated by exogenously expressed wild-type RHOA (**Fig. 4c**), as did a known dominant-negative mutant of RHOA (Thr19Asn) (**Fig. 4a** and data not shown). Gly17Val as well as Thr19Asn RHOA also attenuated actin stress fiber formation in NIH3T3 cells, which was markedly induced by wild-type and Gly14Val RHOA[20] (**Fig. 4d**). Furthermore, the Gly17Val RHOA mutant inhibited the assembly of actin stress fibers in NIH3T3 cells stably expressing wild-type RHOA (**Fig. 4e**). All these data suggest that the Gly17Val mutant functions in a dominant-negative manner with respect to wild-type RHOA.

To investigate the effect of wild-type and Gly17Val RHOA on T cells, we established Jurkat cells inducibly expressing wild-type or Gly17Val RHOA (**Fig. 5a**). When wild-type RHOA was expressed, the proliferation of Jurkat cells was significantly decreased (WT Dox (+) versus Mock DOX (+), $P < 0.001$, days 2–4; **Fig. 5b**), and G1-to-S cell cycle progression was suppressed (**Supplementary Fig. 16**). In contrast, inducibly expressed Gly17Val RHOA did not affect the growth or cell cycle progression of Jurkat cells (**Fig. 5b** and **Supplementary Fig. 16**). We further performed mRNA sequencing analysis to examine the effect of the *RHOA* mutation encoding p.Gly17Val on gene expression, using RNA prepared from Jurkat cells inducibly expressing wild-type or Gly17Val RHOA or mock-transfected cells, as well as RNA from NIH3T3 cells transiently expressing wild-type or Gly17Val RHOA or mock-transfected cells. Gene Set Enrichment Analysis (GSEA)[21,22] demonstrated that the serum response factor (SRF) pathway, known to be activated under RHOA signaling[23], was significantly enriched at a false discovery rate (FDR) *q* value less than 0.25 for cells expressing wild-type RHOA versus mock-transfected cells in both Jurkat and NIH3T3 cells

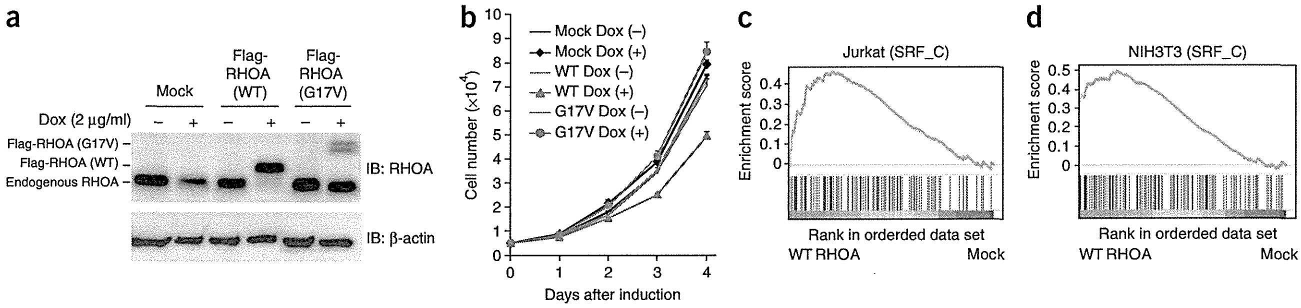

Figure 5 Effect of Gly17Val RHOA on T cells. (**a**) Doxycycline (Dox)-induced expression of wild-type and Gly17Val RHOA in Jurkat cells. A protein blot with antibody to RHOA is shown. β-actin is used as a loading control. (**b**) Proliferation of Jurkat cells inducibly expressing wild-type or Gly17Val RHOA. Absorbance (at 450 nm) was converted to cell number. The mean ± s.d. of quadruplicate experiments is shown. A representative result from three independent experiments is shown. (**c**,**d**) GSEA for Jurkat cells inducibly expressing wild-type or Gly17Val RHOA or mock transfected and NIH3T3 cells transiently expressing wild-type or Gly17Val RHOA or mock transfected ($n = 2$ each). The SRF pathway was differentially enriched in both Jurkat cells (**c**) and NIH3T3 cells (**d**). SRF_C refers to the V$SRF_C gene set.

(**Fig. 5c,d** and **Supplementary Table 12**). The SRF pathway was reported as an essential mediator of T cell development in the thymus[24,25], although we found no clue to its functional relevance in AITL development in the literature. We did not observe enrichment of the SRF pathway in either cell type expressing Gly17Val RHOA compared to mock-transfected cells or cells expressing wild-type RHOA. These findings further support the notion that Gly17Val RHOA is a loss-of-function mutant.

The extremely high frequency and specificity of the *RHOA* mutation encoding p.Gly17Val in AITL and AITL-related PTCL cases unequivocally underscore its major role in the development of these subtypes of PTCL (**Supplementary Fig. 17**). The finding of somatic mutation of *RHOA* in lymphoma, particularly of a mutation with a loss-of-function and/or dominant-negative nature, was rather unexpected because the oncogenic potential of RHOA has been implicated in human cancers[26]. However, several lines of evidence previously suggested a tumor-suppressive role for RHOA in T-lineage cells[26,27]. Moreover, transgenic expression of C3 transferase, an inhibitor of the Rho family of proteins (RHOA, RHOB and RHOC) under the *Lck* promoter has been shown to induce thymic T cell lymphoma in mice[28]. Our observations in Jurkat cells expressing wild-type RHOA are also along these lines. Clearly, further studies are warranted to clarify the molecular pathogenesis mediated by the unique *RHOA* mutation encoding p.Gly17Val in AITL and related PTCL, and such studies might have promising implications for the development of novel diagnostics and therapeutics.

URLs. European Genome-phenome Archive, https://www.ebi.ac.uk/ega/; Genomon-exome, http://genomon.hgc.jp/exome/en/index.html; Picard, http://picard.sourceforge.net/; dbSNP131, http://www.ncbi.nlm.nih.gov/projects/SNP/; 1000 Genomes Project, http://www.1000genomes.org/; MSigDB, http://www.broadinstitute.org/gsea/msigdb.

METHODS

Methods and any associated references are available in the online version of the paper.

Accession codes. Genome sequence data are available at the European Genome-phenome Archive under accession EGAS00001000557.

Note: Any Supplementary Information and Source Data files are available in the online version of the paper

ACKNOWLEDGMENTS

We thank Y. Okoshi, N. Obara, Y. Yokoyama, H. Nishikii, N. Kurita and M. Seki for contributing to sample collection and banking. We also thank Y. Sakashita and T. Takahashi for technical assistance, and S. Narumiya and I. Kitabayashi for efficient discussion. This work was supported by Grants-in-Aid for Scientific Research (KAKENHI) from the Ministry of Education, Culture, Sports, Science and Technology of Japan (22134006 to S.O.; 22130002, 24390241, 25112703 and 25670444 to S.C.; 25461407 to M.S.-Y.) and was supported by the Sagawa Foundation for Promotion of Cancer Research, the Naito Foundation, the Mochida Memorial Foundation for Medical and Pharmaceutical Research (M.S.-Y.).

AUTHOR CONTRIBUTIONS

M.S.-Y. prepared DNA samples, sorted the tumor cells, resequenced the samples, and sorted and integrated information. T.E. analyzed the function of wild-type and mutant RHOA. K.Y. resequenced the samples and contributed to the resequencing data analyses. Y. Shiraishi, E.N., K.C., H.T. and S.M. performed bioinformatics analyses of the resequencing data. R.I. and O.N. created the model structure for mutant RHOA. Y.M., H.M., Y.K., R.N.-M., N.B.T., K.S., T.N., Y.H. and M.N. contributed to sample collection and preparation. N.T., S. Sakata, N.N. and K.T. immunostained specimens and performed pathohistological analyses. Y. Okuno and M.S. contributed to the resequencing. A.S.-O. and Yusuke Sato contributed to mRNA sequencing. K.I., Y. Ohta, J.F., S. Shimizu, T.K., Yuji Sato and T.I. collected samples. M.S.-Y., T.E., K.Y., S.O. and S.C. generated figures and tables, and wrote the manuscript. All authors participated in discussions and interpretation of the data and results.

COMPETING FINANCIAL INTERESTS

The authors declare no competing financial interests.

1. Swerdlow, S.H. *et al. WHO Classification of Tumors of Haematopoietic and Lymphoid Tissues* 4th edn, 306–311 (IARC Press, Lyon, France, 2008).
2. de Leval, L. *et al.* The gene expression profile of nodal peripheral T-cell lymphoma demonstrates a molecular link between angioimmunoblastic T-cell lymphoma (AITL) and follicular helper T (TFH) cells. *Blood* **109**, 4952–4963 (2007).
3. Delhommeau, F. *et al.* Mutation in *TET2* in myeloid cancers. *N. Engl. J. Med.* **360**, 2289–2301 (2009).
4. Mardis, E.R. *et al.* Recurring mutations found by sequencing an acute myeloid leukemia genome. *N. Engl. J. Med.* **361**, 1058–1066 (2009).
5. Lemonnier, F. *et al.* Recurrent *TET2* mutations in peripheral T-cell lymphomas correlate with TFH-like features and adverse clinical parameters. *Blood* **120**, 1466–1469 (2012).
6. Quivoron, C. *et al.* TET2 inactivation results in pleiotropic hematopoietic abnormalities in mouse and is a recurrent event during human lymphomagenesis. *Cancer Cell* **20**, 25–38 (2011).
7. Couronné, L., Bastard, C. & Bernard, O.A. *TET2* and *DNMT3A* mutations in human T-cell lymphoma. *N. Engl. J. Med.* **366**, 95–96 (2012).
8. Cairns, R.A. *et al. IDH2* mutations are frequent in angioimmunoblastic T-cell lymphoma. *Blood* **119**, 1901–1903 (2012).
9. Rodríguez-Pinilla, S.M. *et al.* Peripheral T-cell lymphoma with follicular T-cell markers. *Am. J. Surg. Pathol.* **32**, 1787–1799 (2008).
10. Yoshida, K. *et al.* Frequent pathway mutations of splicing machinery in myelodysplasia. *Nature* **478**, 64–69 (2011).
11. Chapman, M.A. *et al.* Initial genome sequencing and analysis of multiple myeloma. *Nature* **471**, 467–472 (2011).
12. Morin, R.D. *et al.* Frequent mutation of histone-modifying genes in non-Hodgkin lymphoma. *Nature* **476**, 298–303 (2011).
13. Bustelo, X.R., Sauzeau, V. & Berenjeno, I.M. GTP-binding proteins of the Rho/Rac family: regulation, effectors and functions *in vivo*. *Bioessays* **29**, 356–370 (2007).
14. Etienne-Manneville, S. & Hall, A. Rho GTPases in cell biology. *Nature* **420**, 629–635 (2002).
15. Ihara, K. *et al.* Crystal structure of human RhoA in a dominantly active form complexed with a GTP analogue. *J. Biol. Chem.* **273**, 9656–9666 (1998).
16. Shimizu, T. *et al.* An open conformation of switch I revealed by the crystal structure of a Mg^{2+}-free form of RHOA complexed with GDP. Implications for the GDP/GTP exchange mechanism. *J. Biol. Chem.* **275**, 18311–18317 (2000).
17. Reid, T. *et al.* Rhotekin, a new putative target for Rho bearing homology to a serine/threonine kinase, PKN, and rhophilin in the rho-binding domain. *J. Biol. Chem.* **271**, 13556–13560 (1996).
18. Arthur, W.T., Ellerbroek, S.M., Der, C.J., Burridge, K. & Wennerberg, K. XPLN, a guanine nucleotide exchange factor for RhoA and RhoB, but not RhoC. *J. Biol. Chem.* **277**, 42964–42972 (2002).
19. Cheng, Z. *et al.* Luciferase reporter assay system for deciphering GPCR pathways. *Curr. Chem. Genomics* **4**, 84–91 (2010).
20. Ridley, A.J. & Hall, A. The small GTP-binding protein rho regulates the assembly of focal adhesions and actin stress fibers in response to growth factors. *Cell* **70**, 389–399 (1992).
21. Subramanian, A. *et al.* Gene set enrichment analysis: a knowledge-based approach for interpreting genome-wide expression profiles. *Proc. Natl. Acad. Sci. USA* **102**, 15545–15550 (2005).
22. Mootha, V.K. *et al.* PGC-1α–responsive genes involved in oxidative phosphorylation are coordinately downregulated in human diabetes. *Nat. Genet.* **34**, 267–273 (2003).
23. Hill, C.S., Wynne, J. & Treisman, R. The Rho family GTPases RhoA, Rac1, and CDC42Hs regulate transcriptional activation by SRF. *Cell* **81**, 1159–1170 (1995).
24. Mylona, A. *et al.* The essential function for serum response factor in T-cell development reflects its specific coupling to extracellular signal–regulated kinase signaling. *Mol. Cell. Biol.* **31**, 267–276 (2011).
25. Fleige, A. *et al.* Serum response factor contributes selectively to lymphocyte development. *J. Biol. Chem.* **282**, 24320–24328 (2007).
26. Karlsson, R., Pedersen, E.D., Wang, Z. & Brakebusch, C. Rho GTPase function in tumorigenesis. *Biochim. Biophys. Acta* **1796**, 91–98 (2009).
27. Hébert, M. *et al.* Rho-ROCK–dependent ezrin-radixin-moesin phosphorylation regulates Fas-mediated apoptosis in Jurkat cells. *J. Immunol.* **181**, 5963–5973 (2008).
28. Cleverley, S.C., Costello, P.S., Henning, S.W. & Cantrell, D.A. Loss of Rho function in the thymus is accompanied by the development of thymic lymphoma. *Oncogene* **19**, 13–20 (2000).

ONLINE METHODS

Subjects and samples. Samples were obtained from individuals with AITL or PTCL-NOS, as well as from individuals with other mature T cell, mature B cell and myeloid neoplasms, and were used after approval was obtained from the local ethics committees at all participating institutes (**Supplementary Tables 1** and **3**). Informed consent was obtained from all living subjects. High-molecular-weight genomic DNA was extracted from archived specimens that were frozen fresh or after fixation. DNA was also extracted from paraffin-embedded, formalin-fixed samples for targeted amplicon sequencing. Constitutional DNA samples were obtained from buccal swabs, mononuclear cells from apparently tumor-free bone marrow aspirates or peripheral blood. Data on clinical outcomes were available for 71 subjects. Samples of a subcohort of PTCL-NOS cases were reviewed by four expert hematopathologists.

Within PTCL-NOS cases, a subgroup without the typical morphology of AITL but having two or more of the following immunostaining features was designated T_{FH}-like PTCL-NOS[5,9]: (i) positive staining for CD10 in tumor cells, (ii) positive staining for PD-1 in tumor cells, (iii) proliferation of CD21-positive follicular dendritic cells and (iv) the presence of EBER-positive B cells.

Sorting of the tumor cell–enriched fraction and other fractions. $CD4^+$ and $CD8^+$ T cell fractions were purified from skin tumors from subject PTCL159, and $CD4^+$ and $CD8^+$ T cell, $CD19^+$ B cell and $CD14^+$ monocyte cell fractions were purified from pleural effusion cells from subject PTCL160.

The skin tumor from subject PTCL159 was processed into single-cell suspension. Cells were stained with fluorescein isothiocyanate (FITC)-conjugated anti-CD4 antibody (BD Biosciences, 555346) and phycoerythrin (PE)-conjugated anti-CD8 antibody (Dako, clone DK25) and were then fractionated on a FACSAria (BD Biosciences).

Mononuclear cells (MNCs) were isolated from the pleural effusion of subject PTLC160 by Ficoll-Paque density-gradient centrifugation. MNCs were stained with FITC-conjugated anti-CD4 antibody and anti-CD14 antibody (BD Biosciences, 555397), PE-conjugated anti-CD8 antibody and PE-conjugated anti-CD19 antibody (Dako, clone HD37) and were fractionated on a FACSAria.

Whole-exome sequencing. Tumor DNA was extracted from subject biopsy samples infiltrated with lymphoma cells. DNA from either buccal mucosa, bone marrow MNCs without apparent lymphoma infiltration or peripheral blood cells was used for the paired normal control. Whole-exome capture was accomplished through the hybridization of sonicated genomic DNA to the bait cDNA library synthesized on magnetic beads (SureSelect Human All Exon 50Mb or V4 kit, Agilent Technologies). Captured targets were subjected to massively parallel sequencing using a HiSeq 2000 (Illumina) according to the standard protocol for 100-bp paired-end reads.

Detection of candidate somatic mutations was performed using our in-house pipeline for whole-exome sequencing[10] with minor modifications. Briefly, sequencing reads were first aligned to the human reference genome (hg19) using Burrows-Wheeler Aligner (BWA)[29] version 0.5.8 with default parameter settings. PCR duplicates were eliminated using Picard. The number of reads containing SNVs and indels in both tumor and germline samples was determined using SAMtools[30], and the null hypothesis of equal allele frequencies in tumor and germline samples was tested using the two-tailed Fisher's exact test. A variant was adopted as a candidate somatic mutation if it had $P < 0.01$, was observed in bidirectional reads (i.e., in both the plus and minus strands of the reference sequence) and its allele frequency was less than 0.1 in the corresponding germline sample. Finally, the list of candidate somatic mutations was generated by excluding synonymous SNVs and other variants registered in either dbSNP131, the 1000 Genomes Project or our in-house SNP database constructed from 180 individual samples. All candidates were validated by deep sequencing.

Validation of whole-exome analysis. Genomic DNA from tumors and paired normal samples was amplified using the REPLI-g mini kit (Qiagen). Regions that included candidate mutations were amplified by genomic PCR using KOD cox neo (TOYOBO) with a NotI linker attached to each primer (**Supplementary Table 13**). Products were combined, and DNA was purified using the QIAquick PCR Purification kit (Qiagen) and digested with NotI. Digested DNA was purified again, and a 1.5-µg aliquot of purified DNA was ligated with T4 DNA ligase for 5 h, sonicated into ~150-bp fragments on average using Covaris and used for the generation of sequencing libraries, according to a modified Illumina paired-end library protocol. Libraries were then subjected to deep sequencing on a MiSeq (Illumina) according to the standard protocol for 150-bp paired-end reads.

Data processing and variant calling were performed with a set of modifications to the method described in a previous publication[10]. Each read was aligned to the set of targeted sequences from PCR amplification, for which BLAT[31], instead of BWA[29], was used with the –fine option. Mapping information in the .psl format was converted to the .sam format with paired-read information using an in house-generated my_psl2sam script. The script was derived from the psl2sam.pl script distributed with SAMtools. Minor changes were applied to the original script to give the paired-end information upon conversion. Of the successfully mapped reads, the following reads were excluded from further analysis: reads that mapped to multiple sites, reads that mapped with more than four mismatched bases and reads that had more than ten soft-clipped bases. Next, the Estimation_CRME script was run to eliminate strand-specific errors and to exclude cycle-dependent errors. A strand-specific mismatch ratio was calculated for each nucleotide variant for both strands using data for those bases between 11 and 50 cycles. To calculate the frequency of each SNV, all reads were mapped to the target reference sequence using BLAT. The number of mapped reads was differentially enumerated for the dichotomic alleles, i.e., mutant and wild-type alleles. For indels, individual reads were first aligned to each of the wild-type and indel sequences and then assigned to the one with which better alignment was obtained in terms of the number of matched bases. Allele frequency was calculated by enumerating each allele according to those assignments. SNVs comprising equal to or more than 2.0% of total reads of the tumor sample rather than the germline sample at each nucleotide position, if it existed, were adopted as somatic mutations.

Targeted sequencing of the *RHOA*, *TET2*, *IDH1*, *IDH2* and *DNMT3A* genes. Targeted sequencing was performed to determine the mutation rate in a large series of PTCL samples for the *RHOA*, *TET2*, *IDH1*, *IDH2* and *DNMT3A* genes. DNA samples from 79 tumors (46 AITL and 33 PTCL-NOS) and 9 paired bone marrow or peripheral blood cell samples were analyzed, including 6 pairs of tumors and controls analyzed by whole-exome sequencing.

DNA samples were prepared as follows: 61 DNA samples were extracted from fresh frozen biopsy specimens, and 18 DNA samples were extracted from paraformaldehyde-lysine-periodate (PLP)-fixed frozen specimens (46 samples were original DNA, and 33 samples were amplified using the REPLI-g mini kit). All exons of the selected genes were captured with the SureSelect target enrichment system (Agilent Technologies), and massively parallel sequencing was then performed on a HiSeq 2000.

For each sample, all sequencing reads were aligned to hg19 using BWA version 0.5.8 with default parameters. After all duplicated reads and low-quality reads and bases were removed, allele frequencies of SNVs and indels were calculated at each genomic position by enumerating the relevant reads using SAMtools. Initially, all variants showing allele frequencies of >0.02 were extracted and annotated with ANNOVAR[32] for further consideration if they were found in >6 reads out of >10 total reads and appeared in both plus- and minus-strand reads. All synonymous variants, known SNPs in public and private databases, including dbSNP131, the 1000 Genomes Project as of 21 May 2012 and our in-house database, were removed. Candidate mutations whose allele frequencies were <5% were validated by PCR-based deep sequencing using Ion Torrent (Life Technologies).

Deep sequencing using Ion Torrent. Fragmented DNA was prepared in the same manner as described above. Libraries were then subjected to deep sequencing on Ion Torrent according to the standard protocol for 300-bp single-end reads. After excluding reads whose length was >200 bases or <50 bases to reduce sequencing errors, the allele frequency was calculated for each SNV or indel as described above.

Hotspot sequencing to identify *RHOA* mutations encoding p.Gly17Val. Eighty DNA samples from tumors were extracted from unfixed biopsy specimens ($n = 1$), PLP-fixed frozen specimens ($n = 38$) and formalin-fixed, paraffin-embedded specimens ($n = 41$). All samples were original DNA without amplification, except for one sample amplified using the REPLI-g mini kit. Samples were subjected to genomic PCR with tagged PCR primers (**Supplementary Table 14**) and were subsequently prepared using the NEBNext DNA Library-Prep Reagent Set for Illumina (New England BioLabs). Products underwent massively parallel sequencing on a MiSeq according to the manufacturer's protocol. The SNV representing a G-to-T change comprising equal to or more than 2.0% of total reads at the c.G50 nucleotide position of the *RHOA* gene was adopted as the mutation. Methods of data analysis were the same as described above.

Antibodies. Antibodies used for protein blots or immunostaining were mouse anti-RhoA (1:1,000; Cytoskeleton, ARH03), mouse anti–β-actin (1:2,000; Sigma, A5441), mouse anti–DDDDK tag (1:10,000; MBL, M185-3), mouse anti–Myc tag (1:10,000 for WB, 1:500 for IHC; MBL, M192-3), mouse anti-GST tag (1:2,000; MBL, M071-3), rabbit anti-ECT2 (1:1,000; Millipore, 07-1364), goat anti-mouse IgG conjugated to horseradish peroxidase (HRP) (1:10,000; Dako, P0447), goat anti-rabbit IgG conjugated to HRP (1:10,000; Dako, P0448) and Alexa Fluor 647–conjugated goat anti–mouse IgG (1:1,000; Invitrogen, A-21235).

Cell lines and transfection. NIH3T3 cells (American Type Culture Collection) were cultured at 37 °C in low-glucose DMEM (Sigma) supplemented with 10% heat-inactivated FCS and 1% penicillin-streptomycin. Cells were transfected with plasmids using FuGene6 transfection reagent (Promega) according to the manufacturer's protocol. Jurkat cells (European Collection of Cell Cultures) were cultured at 37 °C in RPMI-1640 (Sigma) supplemented with 10% FCS and 1% penicillin-streptomycin.

Mutagenesis and constructs. Human *RHOA* cDNA was isolated by PCR amplification from peripheral blood MNC-derived cDNA. Mutagenesis to create constructs encoding the Gly14Val, Gly17Val, Gly17del, Thr19Asn and Ala161Glu mutants was carried out with the PrimeStar Mutagenesis Basal kit (TaKaRa) according to the manufacturer's instructions. All cDNA-encoded products were tagged at their N terminus with the Flag and/or c-Myc epitope. These constructs were subcloned into the pEF-neo expression vector, the pGCDNsamIRESGFP retroviral vector and the tetracycline-inducible lentivirus-based expression vector CS-TRE-PRE-Ubc-tTA-I2G7 (ref. 33). cDNA encoding the ECT2-GFP fusion protein was kindly provided by T. Ishizaki (Oita University). An N-terminal deletion mutant (residues 414–882) of ECT2 was generated with the PrimeStar Mutagenesis Basal kit. Constructs encoding wild-type and Gly17Val RHOA were subcloned into the pGEX-2tk vector (GE Healthcare). All cDNA sequences were confirmed by Sanger sequencing.

Retrovirus production and generation of stable cell lines. For retrovirus production, each retroviral vector was transfected into 293gp packaging cells with a vesicular stomatitis virus G (VSV-G) expression plasmid[34]. Retrovirus-containing supernatant was used for the transduction of 293gpg cells to establish stable cell lines capable of producing high titers of VSV-G pseudotyped retroviral particles. To establish cell lines stably expressing wild-type or mutant RHOA, NIH3T3 cells were infected with these retroviruses. Infected cells expressing GFP were isolated using a FACSAria. The purity of sorted cell fractions consistently exceeded 95%.

Rhotekin binding assays. The amount of the GTP-bound form of the RHOA protein was measured using the RhoA Activation Assay kit (Cytoskeleton) according to the manufacturer's instructions. Briefly, cell lysate was incubated at 4 °C for 1 h with a GST fusion protein containing the RHO-binding domain of rhotekin (GST-RBD) immobilized on glutathione Sepharose beads. After washing the beads twice with lysis buffer and once with wash buffer provided by the manufacturer, we fractionated bead-bound proteins by 12% SDS-PAGE and immunoblotted with anti-RHOA and anti-Flag antibodies. Total cell lysate was also blotted with anti-RHOA and anti-Flag antibodies to assess the fractional ratios of rhotekin-bound RHOA proteins.

GEF-binding assays. GST-fused wild-type and Gly17Val RHOA proteins were prepared as previously described with minor modification[35]. Briefly, GST-fused wild-type and Gly17Val RHOA proteins were expressed in BL21 competent *Escherichia coli* cells (TaKaRa), which were lysed in lysis buffer (20 mM HEPES, pH 7.5, 150 mM NaCl, 5 mM $MgCl_2$, 1% Triton X-100, 1 mM dithiothreitol and 1 mM phenylmethylsulfonyl fluoride) and subjected to sonication. Lysate was cleared by centrifugation at 20,000*g* for 15 min at 4 °C, incubated with Glutathione Sepharose 4B beads (GE healthcare) for 45 min at 4 °C and washed twice with lysis buffer.

NIH3T3 cells were transiently transfected with a construct expressing the N-terminal deletion mutant of ECT2 by FuGene6. After 48 h, cells were lysed in lysis buffer, cleared by centrifugation and incubated with GST-fused wild-type or Gly17Val RHOA protein bound to Sepharose beads for 2 h. Beads were washed three times with lysis buffer. Bound material was boiled with Laemmli buffer and blotted with anti-GST and anti-ECT2 antibodies.

SRF-RE reporter assays. For the measurement of activity on SRF-RE, luciferase reporter assays were performed using the pGL4.34 reporter vector (Promega), which contains an SRF-RE and a mutant form of the serum response element lacking the ternary complex factor (TCF)-binding domain. SRF-RE was designed to respond to SRF-dependent and TCF-independent signaling such as the signaling that occurs after RhoA activation[19]. NIH3T3 cells were seeded in 24-well plates and cotransfected with pGL4.34 at 40 ng/well, the expression vector pSRα containing β-galactosidase at 20 ng/well and the expression vector pEF-neo containing various *RHOA* cDNA constructs at the concentrations indicated. Luciferase activity was measured at 48 h after transfection, and values were normalized by β-galactosidase activity.

F-actin staining. NIH3T3 cells were transfected with constructs encoding wild-type or mutant RHOA on glass coverslips. After 48 h, cells were fixed with 4% paraformaldehyde in PBS for 15 min at room temperature and permeabilized with 0.5% Triton X-100 in PBS for 10 min. After washing with PBS, cells were incubated with rhodamine phalloidin (100 nM; Cytoskeleton). For double-staining immunohistochemistry, permeabilized cells were blocked with 3% BSA and 0.1% Triton X-100 in PBS. Then, cells were incubated with mouse anti-Myc antibody (1:500 dilution) followed by Alexa Fluor 647–conjugated goat anti–mouse IgG antibody (1:1,000 dilution) and rhodamine phalloidin (100 nM). Nuclei were stained with DAPI. Images were obtained by confocal laser scanning microscopy (Leica).

Lentivirus production and generation of stable cell lines. For lentivirus production, each lentiviral vector was transfected into HEK293T cells with the psPAX2 packaging plasmid and the pMD2.G envelope plasmid. To establish cell lines inducibly expressing wild-type or Gly17Val RHOA, Jurkat cells were infected with these lentiviruses. Infected cells expressing GFP were sorted on a FACSAria. The purity of sorted cell fractions consistently exceeded 95%.

Cell proliferation assays. For cell growth assays, Jurkat cells transduced with lentiviral vectors were incubated in 96-well culture plates, and the absorbance at 450 nm was measured with Cell Counting Kit-8 (Dojindo) according to the manufacturer's instructions.

Cell cycle analysis. Cell cycle distributions were determined by 5-bromo-2′-deoxyuridine (BrdU) and aminoactinomycin D (AAD) incorporation using the APC BrdU Flow kit according to the manufacturer's protocol (BD Pharmingen). Briefly, Jurkat cells were incubated for 30 min in BrdU (10 μM). Then, cells were fixed, permeabilized, treated with DNase and stained with APC-conjugated anti-BrdU antibody and 7-AAD. Flow cytometry was performed on a FACSCalibur cytometer (BD Biosciences), and data were analyzed with FlowJo software (Tree Star).

mRNA sequencing for Jurkat and NIH3T3 cells. Jurkat cells, inducibly expressing wild-type or Gly17Val RHOA, were described above. Wild-type or Gly17Val RHOA protein expression was induced by the addition of 2 μg/ml doxycycline for 2 d ($n = 2$ for each). NIH3T3 cells were transiently transfected with pGCDNsamIRESGFP vector encoding wild-type or Gly17Val RHOA ($n = 2$ for each). After 48 h, GFP-positive cells were sorted by FACSAria.

Total RNA was extracted by RNeasy mini kit (Qiagen) using the RNase-free DNase kit (Qiagen) to reduce contamination from genomic DNA according to the manufacturer's protocol. Libraries for sequencing were prepared using the Illumina TruSeq RNA Sample Preparation kit v2, according to the manufacturer's instructions. Briefly, poly(A)$^+$ RNA was recovered from 1 µg of total RNA using oligo(dT)-coated Sera-Mag magnetic beads. Recovered poly(A)$^+$ RNA was then chemically fragmented. RNA fragments were converted to cDNA using SuperScript II and random primers. The second strand was synthesized using RNase H and DNA polymerase I. cDNA ends were repaired using T4 DNA polymerase, T4 polynucleotide kinase and Klenow DNA polymerase. A single adenosine was added to 3′ ends using Klenow fragment (3′-to-5′ exo minus). Adaptors were attached to cDNA ends using T4 DNA ligase. Fragments were then amplified by ten cycles of PCR using Phusion DNA polymerase. Libraries were validated with an Agilent 2200 TapeStation (Agilent Technologies) and were applied to an Illumina flow cell using the Illumina Cluster Station. Sequencing was performed on a HiSeq 2000 with the paired-end 100-bp read option, according to the manufacturer's instructions.

Reads obtained from RNA sequencing were mapped to the reference transcript and genome using the Genomon-fusion pipeline. For the expression level of each gene, the fragments per kilobase of exon per million mapped reads (FPKM) value was calculated from mapped reads on the gene. GSEA was carried out using GSEA version 2.0. The top ten highest gene sets of normalized enrichment score were listed on the basis of FDR q values (<0.25). Curated gene sets (c2.kegg.version 4.0, c3.tft.version 4.0 and c5.bp.version 4.0) used in this study were obtained from MSigDB collections.

29. Li, H. & Durbin, R. Fast and accurate short read alignment with Burrows-Wheeler transform. *Bioinformatics* **25**, 1754–1760 (2009).
30. Li, H. *et al.* The Sequence Alignment/Map format and SAMtools. *Bioinformatics* **25**, 2078–2079 (2009).
31. Kent, W.J. BLAT—the BLAST-like alignment tool. *Genome Res.* **12**, 656–664 (2002).
32. Wang, K., Li, M. & Hakonarson, H. ANNOVAR: functional annotation of genetic variants from high-throughput sequencing data. *Nucleic Acids Res.* **38**, e164 (2010).
33. Yamaguchi, T. *et al.* Development of an all-in-one inducible lentiviral vector for gene specific analysis of reprogramming. *PLoS ONE* **7**, e41007 (2012).
34. Ory, D.S., Neugeboren, B.A. & Mulligan, R.C. A stable human-derived packaging cell line for production of high titer retrovirus/vesicular stomatitis virus G pseudotypes. *Proc. Natl. Acad. Sci. USA* **93**, 11400–11406 (1996).
35. Guilluy, C., Dubash, A.D. & Garcia-Mata, R. Analysis of RhoA and Rho GEF activity in whole cells and the cell nucleus. *Nat. Protoc.* **6**, 2050–2060 (2011).

The price of drugs for chronic myeloid leukemia (CML) is a reflection of the unsustainable prices of cancer drugs: from the perspective of a large group of CML experts

Experts in Chronic Myeloid Leukemia

As a group of more than 100 experts in chronic myeloid leukemia (CML), we draw attention to the high prices of cancer drugs, with the particular focus on the prices of approved tyrosine kinase inhibitors for the treatment of CML. This editorial addresses the multiple factors involved in cancer drug pricing and their impact on individual patients and health care policies, and argues for the need to (1) lower the prices of cancer drugs to allow more patients to afford them and (2) maintain sound long-term health care policies. (*Blood.* 2013;121(22):4439-4442)

The doctrine of *justum pretium*, or just price, refers to the "fair value" of commodities. In deciding the relationship between price and worth (or value), it advocates that, by moral necessity, price must reflect worth. This doctrine may be different from the doctrine of free market economies where prices reflect "what the market bears," or what one is willing to pay for a product. Which doctrine is better? One could argue that when a commodity affects the lives or health of individuals, just price should prevail because of the moral implications. Examples include the price of bread during famines, polio vaccine, ivermectin for river blindness (provided for free by Merck and estimated to have saved the vision of 30 million individuals), and treatments of chronic medical conditions (cardiovascular, hypertension, diabetes, tuberculosis, multiple sclerosis, etc). When commodities are not essential to life or suffering, what the market will bear is appropriate (competition will take care of price) because it is not restrained by ethical considerations. Examples include the price of a Picasso painting, a luxury cruise, a 2-week vacation in New York (or 4 weeks in Houston), a Bentley car, a Brioni suit, etc.

Through positive collaborations with Pharma, experts in chronic myelogenous leukemia (CML) have been fortunate to have 3 drugs approved by the US Food and Drug Administration (FDA) in 2012 for the treatment of CML: bosutinib, ponatinib, and omacetaxine. This is in addition to 3 others approved in the last decade: imatinib, dasatinib, and nilotinib. The 3 new drugs, however, have been priced at astronomical levels: ponatinib at $138 000 per year, omacetaxine at $28 000 for induction and $14 000 per maintenance course, and bosutinib at ~$118 000 per year.[1]

Cancer drug prices have been discussed recently by some financial analysts and tend to be discussed whenever new cancer drugs are approved. This Forum reflects the views of a large group of CML experts who believe that the current prices of CML drugs (1) are too high, (2) are unsustainable, (3) may compromise access of needy patients to highly effective therapy, and (4) are harmful to the sustainability of our national health care systems. These concerns reflect the spiraling prices of cancer drugs in general. Of the 12 drugs approved by the FDA for various cancer indications in 2012, 11 were priced above $100 000 per year. Cancer drug prices have almost doubled from a decade ago, from an average of $5000 per month to >$10 000 per month.[2]

Innovation and discoveries must be rewarded. Pharmaceutical companies that invest in research and development and discover new lifesaving drugs should benefit from healthy revenues. The cost for bringing a new cancer drug to market is reported to be ~$1 billion.[3] This much-argued-about figure, which some independent experts put as low as $60 to 90 million,[4] includes the cost of development of the new (successful) drug and all other drugs that failed during development, and ancillary expenses including the cost of conducting the clinical trials required for approval, bonuses, salaries, infrastructures, and advertising among others. In other words, once a company sells about a billion dollars of a drug, most of the rest is profit.

How are the prices of cancer drugs decided? Of the many complex factors involved, price often seems to follow a simple formula: start with the price for the most recent similar drug on the market and price the new one within 10% to 20% of that price (usually higher). This is what happened with imatinib, priced in 2001 at $2200 per month, based on the price of interferon, which was then the standard treatment.[5]

If drug price reflects value, then it should be proportional to the benefit to patients in objective measures, such as survival prolongation, degree of tumor shrinkage, or improved quality of life. For many tumors, drug prices do not reflect these end points because most anticancer drugs provide minor survival benefits, if at all. For example, in pancreatic cancer, where the median survival is 6 months, a new drug that may prolong survival by 2 months and is priced at $100 000 per year will cost $67 000 over 8 months survived, or $33 500 per additional month lived, equivalent to $400 000 per additional year lived. Similar calculations can be made for other cancers depending on the expected median survival, additional time lived, and therefore the price of an additional year lived. By these measures, the price of cetuximab was valued at ~$800 000 per

---

Submitted March 12, 2013; accepted March 27, 2013. Prepublished online as *Blood* First Edition paper, April 25, 2013; DOI 10.1182/blood-2013-03-490003.

Experts in Chronic Myeloid Leukemia contributed equally to this study and are cited in "Appendix."

The online version of this article contains a data supplement.

The publication costs of this article were defrayed in part by page charge payment. Therefore, and solely to indicate this fact, this article is hereby marked "advertisement" in accordance with 18 USC section 1734.